

Bifurcated Backbone Strategy for RGB-D Salient Object Detection

Yingjie Zhai*, Deng-Ping Fan*, Jufeng Yang, Ali Borji, Ling Shao, *Senior Member, IEEE*, Junwei Han, *Senior Member, IEEE*, and Liang Wang, *Fellow, IEEE*

Abstract—Multi-level feature fusion is a fundamental topic in computer vision. It has been exploited to detect, segment and classify objects at various scales. When multi-level features meet multi-modal cues, the optimal feature aggregation and multi-modal learning strategy become a hot potato. In this paper, we leverage the inherent multi-modal and multi-level nature of RGB-D salient object detection to devise a novel cascaded refinement network. In particular, first, we propose to regroup the multi-level features into teacher and student features using a bifurcated backbone strategy (BBS). Second, we introduce a depth-enhanced module (DEM) to excavate informative depth cues from the channel and spatial views. Then, RGB and depth modalities are fused in a complementary way. Our architecture, named **Bifurcated Backbone Strategy Network (BBS-Net)**, is simple, efficient, and backbone-independent. Extensive experiments show that *BBS-Net* significantly outperforms eighteen SOTA models on eight challenging datasets under five evaluation measures, demonstrating the superiority of our approach (~4% improvement in S-measure *vs.* the top-ranked model: DMRA-iccv2019). In addition, we provide a comprehensive analysis on the generalization ability of different RGB-D datasets and provide a powerful training set for future research.

Index Terms—RGB-D salient object detection, bifurcated backbone strategy, multi-level features, cascaded refinement.

1 INTRODUCTION

THE goal of salient object detection (SOD) is to find and segment the most visually prominent object(s) in an image [2], [3]. Over the last decade, SOD has attracted significant attention due to its widespread applications in object recognition [4], content-based image retrieval [5], image segmentation [6], image editing [7], video analysis [8], [9], and visual tracking [10], [11]. Traditional SOD algorithms [12], [13] are typically based on handcrafted features and fall short in capturing high-level semantic information (see also [14], [15]). Recently, convolutional neural networks (CNNs) have been used for RGB SOD [16], [17], achieving better performance compared to the traditional methods.

However, the performance of RGB SOD models tends to drastically decrease when faced with certain complex scenarios (*e.g.*, cluttered backgrounds, multiple objects, varying illuminations, transparent objects, *etc*) [18]. One of the most important reasons behind these failure cases may be the lack of depth information, which is critical for saliency prediction. For example, an object with less texture but closer to the camera will be more salient than an object with more

texture but farther away. Depth maps contain abundant spatial structure and layout information [19], providing geometrical cues for improving the performance of SOD. Besides, depth information can easily be obtained using popular devices, *e.g.*, stereo cameras, Kinect and smartphones, which are becoming increasingly more ubiquitous. Therefore, various algorithms (*e.g.*, [20], [21]) have been proposed to solve the SOD problem by combining RGB and depth information (*i.e.*, RGB-D SOD).

To efficiently integrate RGB and depth cues for SOD, researchers have explored different but complementary multi-modal and multi-level strategies [22]–[24] and have achieved encouraging results. However, existing RGB-D SOD methods still have to solve the following challenges to make further progress:

(1) **Effectively aggregating multi-level features.** As discussed in [16], teacher features¹ contain rich semantic macro information and can serve as strong guidance for locating salient objects, while student features provide affluent micro details that are beneficial for refining object edges. Therefore, current RGB-D SOD methods use either a dedicated aggregation strategy [19], [21] or a progressive merging process [25], [26] to leverage multi-level features. However, because they directly fuse multi-level features without considering level-specific characteristics, these operations suffer from the inherent problem of noisy low-level features [18], [27]. As a result, several methods are easily confused by the background (*e.g.*, first and second rows in Fig. 1).

(2) **Excavating informative cues from the depth modality.** Previous algorithms usually regard the depth map as a fourth-channel input [31], [32] of the original three-channel

- Yingjie Zhai and Deng-Ping Fan contribute equally to this work.
- Yingjie Zhai, Deng-Ping Fan and Jufeng Yang are with College of Computer Science, Nankai University. (Email: zhaiyingjie@163.com, dengfan@gmail.com, yangjufeng@nankai.edu.cn)
- Ali Borji is with HCL America, NYC, USA. (Email: aliborji@gmail.com)
- Ling Shao is with the Mohamed bin Zayed University of Artificial Intelligence, Abu Dhabi, UAE, and also with the Inception Institute of Artificial Intelligence, Abu Dhabi, UAE. (Email: ling.shao@ieee.org)
- Junwei Han is with School of Automation, Northwestern Polytechnical University, China. (Email: junweihan2010@gmail.com)
- Liang Wang is with the National Laboratory of Pattern Recognition, CAS Center for Excellence in Brain Science and Intelligence Technology, Institute of Automation, Chinese Academy of Sciences, Beijing 100190, China. (Email: wangliang@nlpr.ia.ac.cn)
- A preliminary version of this work has appeared in ECCV 2020 [1].
- Corresponding author: Jufeng Yang.

1. Note that we use the terms high-level features & low-level features and teacher features & student features interchangeably.

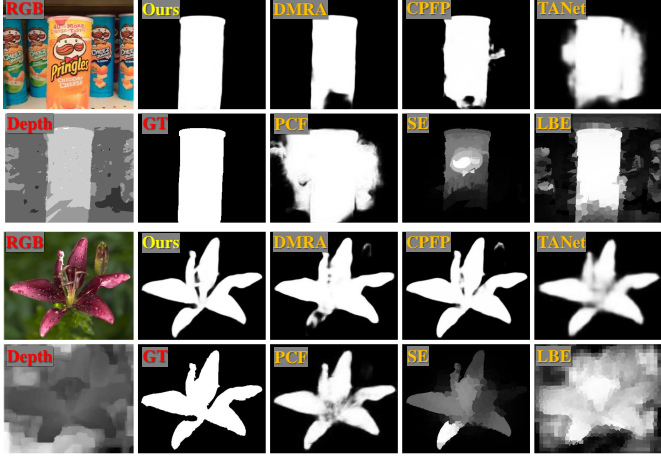


Fig. 1. Saliency maps of state-of-the-art (SOTA) CNN-based methods (*i.e.*, DMRA [19], CPFP [21], TANet [18], PCF [22] and Ours) and methods based on handcrafted features (*i.e.*, SE [28] and LBE [29]). Our method generates higher-quality saliency maps and suppresses background distractors in challenging scenarios (top: complex background; bottom: depth with noise).

RGB image, or fuse RGB and depth features by simple summation [33], [34] and multiplication [35], [36]. However, these methods treat depth and RGB information from the same perspective and ignore the fact that RGB images capture color and texture, whereas depth maps capture the spatial relations among objects. Due to this modality difference, the above-mentioned simple combination methods are not very efficient. Further, depth maps are often of low quality, which introduces randomly distributed errors and redundancy into the network [37]. For example, the depth map in the last row of Fig. 1 is blurry and noisy. As a result, many methods (*e.g.*, the top-ranked model DMRA [19]) fail to detect the full extent of the salient object.

To address the above issues, we propose a novel **Bifurcated Backbone Strategy Network (BBS-Net)** for RGB-D SOD. The proposed method exploits multi-level features in a cascaded refinement way to suppress distractors in the lower layers. This strategy is based on the observation that teacher features provide discriminative semantic information without redundant details [16], [27], which may contribute significantly to eliminating the lower-layer distractors. As shown in Fig. 2 (b), BBS-Net contains two cascaded decoder stages: (1) Cross-modal teacher features are integrated by the first cascaded decoder $CD1$ to predict an initial saliency map S_1 . (2) Student features are refined by an element-wise multiplication with the initial saliency map S_1 and are then aggregated by another cascaded decoder $CD2$ to produce the final saliency map S_2 . To fully capture the informative cues in the depth map and improve the compatibility of RGB and depth features, we further introduce a depth-enhanced module (DEM). This module exploits the inter-channel and spatial relations of the depth features and discovers informative depth cues. Our main contributions are summarized as follows:

- **We propose a powerful Bifurcated Backbone Strategy Network (BBS-Net)** to deal with multiple complicated real-world scenarios in RGB-D SOD. To address the

long-overlooked problem of noise in low-level features decreasing the performance of saliency models, we carefully explore the characteristics of multi-level features in a bifurcated backbone strategy (BBS), *i.e.*, features are split into two groups, as shown in Fig. 2 (b). In this way, noise in student features can be eliminated effectively by the saliency map generated from teacher features.

- We further introduce a **depth-enhanced module (DEM)** in *BBS-Net* to enhance the depth features before merging them with the RGB features. The DEM module concentrates on the most informative parts of depth maps by two sequential attention operations. We leverage the attention mechanism to excavate important cues from the depth features of multiple side-out layers. This module is simple but has proven effective for fusing RGB and depth modalities in a complementary way.
- We conduct a comprehensive comparison with 18 **SOTA methods** using various metrics (*e.g.*, max F-measure, MAE, S-measure, max E-measure, and PR curves). Experimental results show that *BBS-Net* outperforms all of these methods on eight public datasets, by a large margin. In terms of the quality of predicted saliency maps, *BBS-Net* generates maps with sharper edges and fewer background distractors compared to existing models.
- We conduct a number of cross-dataset experiments to evaluate the quality of current popular RGB-D datasets and introduce a training set with high generalization ability for fair comparison and future research. Current RGB-D methods train their networks using the fixed training-test splits of different datasets, without exploring the difficulties of those datasets. To the best of our knowledge, we are the first to investigate this important but overlooked problem in the area of RGB-D SOD.

This work is based on our previous conference paper [1] and extends it significantly in four ways: 1) We provide more details and experiments regarding our *BBS-Net* model, including motivation, feature visualizations, experimental settings, *etc.* 2) We investigate several previously unexplored issues, including cross-dataset generalization ability, post-processing methods, *etc.* 3) To further demonstrate our model performance, we conduct several comprehensive experiments over the recently released dataset, DUT [19]. 4) We provide several failure cases of *BBS-Net*, perform in-depth analyses and draw several novel conclusions which are critical in developing more powerful models in the future. We are hopeful that our study will provide deep insights into the underlying design mechanisms of RGB-D SOD, and will spark novel ideas. The complete algorithm implementations, benchmark results, and post-processing toolbox have been made publicly available at <https://github.com/zjwuyan/BBS-Net>.

2 RELATED WORKS

2.1 Salient Object Detection

Over the past several decades, SOD [38]–[40] has garnered significant research attention due to its diverse applications [41]–[43]. In early years, SOD methods were mainly based on intrinsic prior knowledge such as center-surround

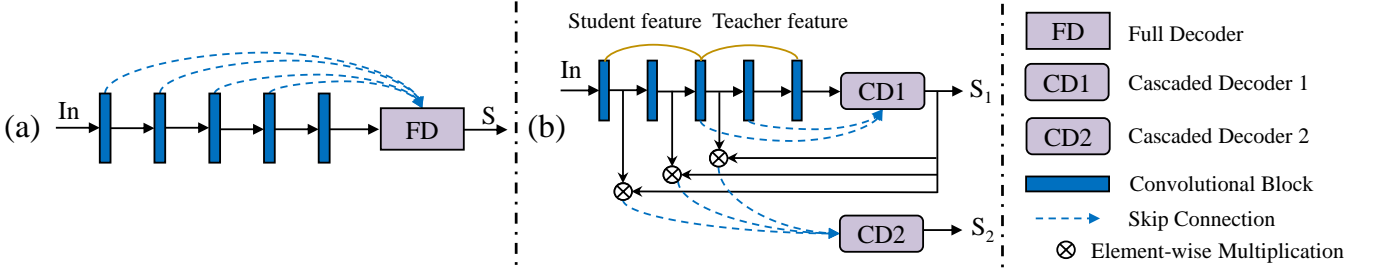


Fig. 2. (a) Existing multi-level feature aggregation methods for RGB-D SOD [18], [19], [21], [22], [25], [26], [30]. (b) In this paper, we adopt a bifurcated backbone strategy (BBS) to split the multi-level features into student and teacher features. The initial saliency map S_1 is utilized to refine the student features to effectively suppress distractors. Then, the refined features are passed to another cascaded decoder to generate the final saliency map S_2 .

color contrast [44], global region contrast [12], background prior [45] and appearance similarity [46]. However, these methods heavily rely on heuristic saliency cues and low-level handcrafted features, thus lacking the guidance of high-level semantic information.

Recently, to solve this problem, deep learning based methods [47]–[51] have been explored, exceeding handcrafted features based methods in complex scenarios. These deep methods [52] usually leverage CNNs to extract multi-level multi-scale features from RGB images and then aggregate them to predict the final saliency map. Such multi-level multi-scale features [53], [54] can help the model better understand the contextual and semantic information to generate high-quality saliency maps. Besides, since image-based SOD may be limited in some real-world applications such as video captioning [55], autonomous driving [56] and robotic interaction [57], SOD algorithms [8], [9] have also been explored for video analysis.

To further break through the limits of deep models, researchers have also proposed to excavate edge information [58] to guide prediction. These methods use an auxiliary boundary loss to improve the training and representative ability of segmentation tasks [59]–[61]. With the auxiliary guidance from the edge information, deep models can predict maps with finer and sharper edges. In addition to edge guidance, another useful type of auxiliary information are depth maps, which capture the spatial distance information. These are the main focus of this paper.

2.2 RGB-D Salient Object Detection

- **Traditional Models.** Previous algorithms for RGB-D SOD mainly rely on extracting handcrafted features [35], [36] from RGB and depth images. Contrast-based cues, including edge, color, texture and region, are largely utilized by these methods to compute the saliency of a local region. For example, Desingh *et al.* [62] adopted the region-based contrast to calculate contrast strengths for the segmented regions. Ciptadi *et al.* [63] used surface normals and color contrast to compute saliency. However, the local contrast methods are easily disturbed by high-frequency content [64], since they mainly rely on the boundaries of salient objects. Therefore, some algorithms, such as spatial prior [35], global contrast [65], and background prior [66],

proposed to compute saliency by combining both local and global information.

To combine saliency cues from RGB and depth modalities more effectively, researchers have explored multiple fusion strategies. Some methods [31], [32] process RGB and depth images together by regarding depth maps as fourth-channel inputs (early fusion). This operation is simple but does not achieve reliable results, since it disregards the differences between the RGB and depth modalities. Therefore, some algorithms [33], [36] extract the saliency information from the two modalities separately by first leveraging two backbones to predict saliency maps and then fusing the saliency results (late fusion). Besides, to enable the RGB and depth modalities share benefits, other methods [29], [67] fuse RGB and depth features in a middle stage and then produce the corresponding saliency maps (middle fusion). Deep models also use the above three fusion strategies, and our method falls under the middle fusion category.

- **Deep Models.** Early deep methods [64], [66] compute saliency confidence scores by first extracting handcrafted features, and then feeding them to CNNs. However, these algorithms need the low-level handcrafted features to be manually designed as input, and thus cannot be trained in an end-to-end manner. More recently, researchers have begun to extract deep RGB and depth features using CNNs in a bottom-up fashion [69]. Unlike handcrafted features, deep features contain a lot of contextual and semantic information, and can thus better capture representations of the RGB and depth modalities. These methods have achieved encouraging results, which can be attributed to two important aspects of feature fusion. One is their extraction and fusion of multi-level and multi-scale features from different layers, while the other is the mechanism by which the two different modalities (RGB and depth) are combined.

Various architectures have been designed to effectively integrate the multi-scale features. For example, Liu *et al.* [25] obtained saliency map outputs from each side-out features by feeding a four-channel RGB-D image into a single backbone (single stream). Chen *et al.* [22] leveraged two independent networks to extract RGB and depth features respectively, and then combined them in a progressive merging way (double stream). Furthermore, to learn supplementary features, [18] designed a three-stream network consisting of two modality-specific streams and a parallel cross-modal

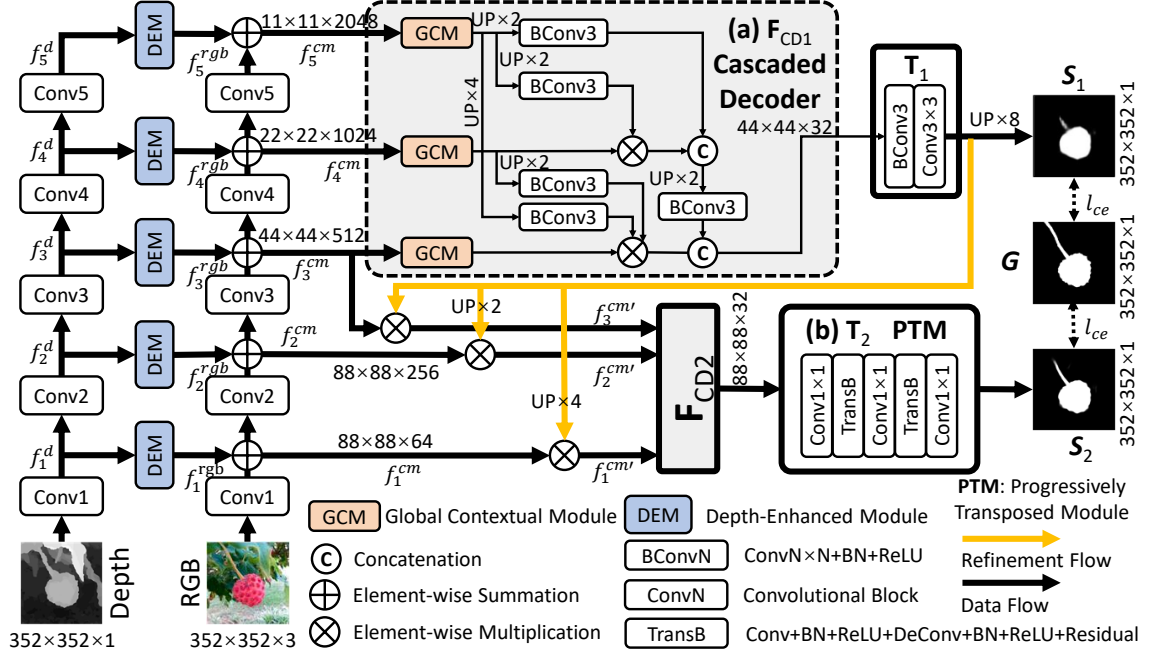


Fig. 3. **Overall architecture of the proposed BBS-Net.** Feature Extraction: ‘Conv1’~‘Conv5’ denote different layers from ResNet-50 [68]. Multi-level features ($f_1^d \sim f_5^d$) from the depth branch are enhanced by the DEM and are then fused with features (*i.e.*, $f_1^{rgb} \sim f_5^{rgb}$) from the RGB branch. Stage 1: cross-modal teacher features ($f_3^{cm} \sim f_5^{cm}$) are first aggregated by the cascaded decoder (a) to produce the initial saliency map S_1 . Stage 2: Then, student features ($f_1^{cm} \sim f_3^{cm}$) are refined by the initial saliency map S_1 and are integrated by another cascaded decoder to predict the final saliency map S_2 . See § 3 for details.

distillation stream to exploit complementary cross-modal information in the bottom-up feature extraction process (three streams). Depth maps are sometimes low-quality and may thus contain significant noise or misleading information, which greatly decreases the performance of SOD models. To address this issue, Zhao *et al.* [21] proposed a contrast-enhanced network to improve the quality of depth maps using the contrast prior. Fan *et al.* [37] designed a depth depurator unit to evaluate the quality of depth maps and filter out the low-quality ones automatically. Three recent works have explored uncertainty [70], depth prediction [71] and a joint learning strategy [72] for saliency detection and achieved reasonable performance. There were also some concurrent works published in recent top conferences (*e.g.*, ECCV [73]–[75]). Discussing these works in detail is beyond the scope of this article. Please refer to the online benchmark (<http://dpfan.net/d3netbenchmark/>) and the latest survey [76] for more details.

Different from the above works, which overlook the intrinsic noise in low-level features, we devise a bifurcated backbone strategy with a cascaded refinement mechanism, thereby effectively suppressing the noise in student features with the guidance of the teacher features (the last column in Fig. 8). Details of our approach are described next.

3 PROPOSED METHOD

3.1 Overview

Current popular RGB-D SOD models directly integrate multi-level features using a single decoder (Fig. 2 (a)). In contrast, the network flow of the proposed BBS-Net (Fig. 3) explores a bifurcated backbone strategy. In § 3.2, we first

detail the proposed bifurcated backbone strategy with the cascaded refinement mechanism. Then, to fully excavate informative cues from the depth map, we introduce a new depth-enhanced module in § 3.3.

3.2 Bifurcated Backbone Strategy (BBS)

Our cascaded refinement mechanism leverages the rich semantic information in high-level cross-modal features to suppress background distractors. To support such a feat, we devise a bifurcated backbone strategy (BBS). It divides the multi-level cross-modal features into two groups, *i.e.*, $G_1 = \{Conv1, Conv2, Conv3\}$ and $G_2 = \{Conv3, Conv4, Conv5\}$, where $Conv3$ is the split point. The original multi-scale information is well preserved by each group.

• Cascaded Refinement Mechanism. To effectively leverage the characteristics of the two groups’ features, we train the network using a cascaded refinement mechanism. This mechanism first generates an initial saliency map with three cross-modal teacher features (*i.e.*, G_2) and then enhances the details of the initial saliency map S_1 with three cross-modal student features (*i.e.*, G_1), which are refined by the initial saliency map. This is based on the observation that high-level features contain rich semantic information that helps locate salient objects, while low-level features provide micro-level details that are beneficial for refining the boundaries. In other words, by exploring the characteristics of the multi-level features, this strategy can efficiently suppress noise in low-level cross-modal features, and can produce the final saliency map through a progressive refinement.

Specifically, we first merge RGB and depth features processed by the DEM (Fig. 4) to obtain the cross-modal

features $\{f_i^{cm}; i = 1, 2, \dots, 5\}$. In stage one, the three cross-modality teacher features (i.e., $f_3^{cm}, f_4^{cm}, f_5^{cm}$) are aggregated by the first cascaded decoder, which is denoted as:

$$S_1 = \mathbf{T}_1(\mathbf{F}_{CD1}(f_3^{cm}, f_4^{cm}, f_5^{cm})), \quad (1)$$

where \mathbf{F}_{CD1} is the first cascaded decoder, S_1 is the initial saliency map, and \mathbf{T}_1 represents two simple convolutional layers that transform the channel number from 32 to 1. In stage two, we leverage the initial saliency map S_1 to refine the three cross-modal student features, which is defined as:

$$f_i^{cm'} = f_i^{cm} \odot S_1, \quad (2)$$

where $f_i^{cm'} (i \in \{1, 2, 3\})$ represents the refined features and \odot denotes the element-wise multiplication. After that, the three refined student features are aggregated by another decoder followed by a progressively transposed module (PTM), which is formulated as:

$$S_2 = \mathbf{T}_2(\mathbf{F}_{CD2}(f_1^{cm'}, f_2^{cm'}, f_3^{cm'})), \quad (3)$$

where \mathbf{F}_{CD2} is the second cascaded decoder, S_2 denotes the final saliency map, and \mathbf{T}_2 represents the PTM module.

• Cascaded Decoder. After computing the two groups of multi-level cross-modal features ($\{f_i^{cm}, f_{i+1}^{cm}, f_{i+2}^{cm}\}, i \in \{1, 3\}$), which are a fusion of the RGB and depth features from multiple layers, we need to efficiently leverage the multi-scale multi-level information in each group to carry out the cascaded refinement. Therefore, we introduce a light-weight cascaded decoder [27] to integrate the two groups of multi-level cross-modal features. As shown in Fig. 3 (a), the cascaded decoder consists of three global context modules (GCM) and a simple feature aggregation strategy. The GCM is refined from the RFB module [77]. Specifically, it contains an additional branch to enlarge the receptive field and a residual connection [68] to preserve the information. The GCM module thus includes four parallel branches. For all of these branches, a 1×1 convolution is first applied to reduce the channel size to 32. Then, for the k^{th} ($k \in \{2, 3, 4\}$) branch, a convolution operation with a kernel size of $2k - 1$ and dilation rate of 1 is applied. This is followed by another 3×3 convolution operation with the dilation rate of $2k - 1$. We aim to excavate the global contextual information from the cross-modal features. Next, the outputs of the four branches are concatenated together and a 1×1 convolution operation is then applied to reduce the channel number to 32. Finally, the concatenated features form a residual connection with the input features. The GCM module operation in the two cascaded decoders is denoted by:

$$f_i^{gcm} = \mathbf{F}_{GCM}(f_i). \quad (4)$$

To further improve the representations of cross-modal features, we leverage a pyramid multiplication and concatenation feature aggregation strategy to aggregate the cross-modal features ($\{f_i^{gcm}, f_{i+1}^{gcm}, f_{i+2}^{gcm}\}, i \in \{1, 3\}$). As illustrated in Fig. 3 (a), first, each refined feature f_i^{gcm} is updated by multiplying it with all higher-level features:

$$f_i^{gcm'} = f_i^{gcm} \odot \Pi_{k=i+1}^{k_{max}} \text{Conv}(\mathbf{F}_{UP}(f_k^{gcm})), \quad (5)$$

in which $i \in \{1, 2, 3\}$, $k_{max} = 3$ or $i \in \{3, 4, 5\}$, $k_{max} = 5$. \mathbf{F}_{UP} represents the upsampling operation if the features

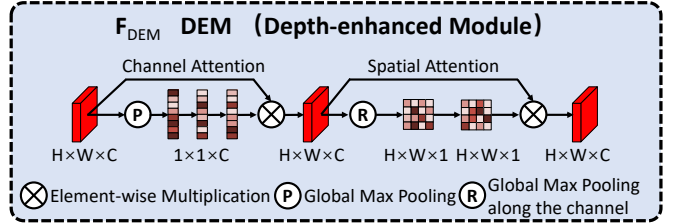


Fig. 4. Architecture of the depth-enhanced module (DEM).

are not of the same scale. \odot represents the element-wise multiplication, and $\text{Conv}(\cdot)$ represents the standard 3×3 convolution operation. Then, the updated features are integrated by a progressive concatenation strategy to produce the output:

$$S = \mathbf{T} \left(\left[f_k^{gcm'}; \text{Conv} \left(\mathbf{F}_{UP} \left[f_{k+1}^{gcm'}; \text{Conv} \left(\mathbf{F}_{UP} \left(f_{k+2}^{gcm'} \right) \right) \right] \right) \right] \right), \quad (6)$$

where S is the predicted saliency map, $[x; y]$ denotes the concatenation operation of x and y , and $k \in \{1, 3\}$. In the first stage, \mathbf{T} denotes two sequential convolutional layers (i.e., \mathbf{T}_1), while, for the second stage, it represents the PTM module (i.e., \mathbf{T}_2). The scale of the output of the second decoder is 88×88 , which is $1/4$ of the ground-truth (352×352), so directly upsampling the output to the size of the ground-truth will lose some details. To address this issue, we propose a simple yet effective progressively transposed module (PTM, Fig. 3 (b)) to generate the final predicted map (S_2) in a progressive upsampling way. It consists of two residual-based transposed blocks [78] and three sequential 1×1 convolutions. Each residual-based transposed block contains a 3×3 convolution and a residual-based transposed convolution.

Note that the proposed cascaded refinement mechanism is different from the recent refinement strategies CRN [79], SRM [80], R3Net [81], and RFCN [17] in its usage of the initial map and multi-level features. The obvious difference and advantage of the proposed design is that our model only requires one round of saliency refinement to produce a good saliency map, while CRN, SRM, R3Net, and RFCN all need more iterations, which increases both the training time and computational resources. Besides, the proposed cascaded mechanism is also different from CPD [27] in that it exploits both the details in student features and the semantic information in teacher features, while suppressing the noise in the student features at the same time.

3.3 Depth-Enhanced Module (DEM)

To effectively fuse the RGB and depth features, two main problems need to be solved: a) the compatibility of RGB and depth features needs to be improved due to the intrinsic modality difference, and b) the redundancy and noise in low-quality depth maps must be reduced. Inspired by [82], we design a depth-enhanced module (DEM) to address the issues by improving the compatibility of multi-modal features and excavating informative cues from the depth features.

Specifically, let f_i^{rgb}, f_i^d represent the feature maps of the i^{th} ($i \in 1, 2, \dots, 5$) side-out layer from the RGB and

depth branches, respectively. As shown in Fig. 3, each DEM is added before each side-out feature map from the depth branch to enhance the compatibility of the depth features. This side-out process improves the saliency representation of depth features and, at the same time, preserves the multi-level multi-scale information. The fusion process of the two modalities is depicted as:

$$f_i^{cm} = f_i^{rgb} + \mathbf{F}_{DEM}(f_i^d), \quad (7)$$

where f_i^{cm} denotes the cross-modal features of the i^{th} layer. As shown in Fig. 4, the DEM module contains a sequential channel attention operation and a spatial attention operation, which are formulated as:

$$\mathbf{F}_{DEM}(f_i^d) = \mathbf{S}_{att}(\mathbf{C}_{att}(f_i^d)), \quad (8)$$

in which $\mathbf{C}_{att}(\cdot)$ and $\mathbf{S}_{att}(\cdot)$ represent the spatial and channel attention operations, respectively. More specifically, the channel attention is implemented as:

$$\mathbf{C}_{att}(f) = \mathbf{M}(\mathbf{P}_{max}(f)) \otimes f, \quad (9)$$

where $\mathbf{P}_{max}(\cdot)$ denotes the global max pooling operation for each feature map, $\mathbf{M}(\cdot)$ represents a multi-layer (two-layer) perceptron, f denotes the input feature map, and \otimes is the multiplication by the dimension broadcast. The spatial attention is denoted as:

$$\mathbf{S}_{att}(f) = \text{Conv}(\mathbf{R}_{max}(f)) \odot f, \quad (10)$$

where $\mathbf{R}_{max}(\cdot)$ is the global max pooling operation for each point in the feature map along the channel axis. The proposed depth enhanced module is different from previous RGB-D algorithms, which fuse the multi-level cross-modal features by direct concatenation [18], [22], [26], enhance the multi-level depth features by a simple convolutional layer [19] or improve the depth map by contrast prior [21]. To the best of our knowledge, we are the first to introduce the attention mechanism to excavate informative cues from depth features in multiple side-out layers. Our experiments (see Tab. 7 and Fig. 9) demonstrate the effectiveness of our approach in improving the compatibility of multi-modal features.

Besides, the spatial and channel attention mechanisms are different from the operation proposed in [82]. Based on the fact that SOD aims at finding the most prominent objects in an image, we only leverage a single global max pooling [83] to excavate the most critical cues in depth features, which reduces the complexity of the module.

3.4 Implementation Details

• **Training Loss.** Let \mathcal{H} and \mathcal{W} denote the height and width of the input images. Given the input RGB image $X \in \mathbb{R}^{\mathcal{H} \times \mathcal{W} \times 3}$ and its corresponding depth map $D \in \mathbb{R}^{\mathcal{H} \times \mathcal{W} \times 1}$, our model predicts an initial saliency map $S_1 \in [0, 1]^{\mathcal{H} \times \mathcal{W} \times 1}$ and a final saliency map $S_2 \in [0, 1]^{\mathcal{H} \times \mathcal{W} \times 1}$. Let $G \in \{0, 1\}^{\mathcal{H} \times \mathcal{W} \times 1}$ denote the binary ground-truth saliency map. We jointly optimize the two cascaded stages by defining the total loss:

$$\mathcal{L} = \alpha \ell_{ce}(S_1, G) + (1 - \alpha) \ell_{ce}(S_2, G), \quad (11)$$

in which ℓ_{ce} represents the binary cross entropy loss [21] and $\alpha \in [0, 1]$ controls the trade-off between the two parts of the losses. The ℓ_{ce} is computed as:

$$\ell_{ce}(S, G) = G \log S + (1 - G) \log(1 - S), \quad (12)$$

where S is the predicted saliency map.

• **Training Protocol.** We use the PyTorch [87] framework to implement our model on a single 1080Ti GPU. Parameters of the backbone network (ResNet-50 [68]) are initialized from the model pre-trained on ImageNet [88]. We discard the last pooling and fully connected layers of ResNet-50 and leverage each middle output of the five convolutional blocks as the side-out feature maps. The two branches do not share weights and the only difference between them is that the depth branch has the input channel number set to one. Other parameters are initialized using the default PyTorch settings. The Adam algorithm [89] is used to optimize our model. We set the initial learning rate to 1e-4 and divide it by 10 every 60 epochs. The input RGB and depth images are resized to 352×352 for both the training and test phases. We augment all the training images using multiple strategies (*i.e.*, random flipping, rotating and border clipping). It takes about ten hours to train the model with a mini-batch size of 10 for 150 epochs. Our experiments show that the model is robust to the hyper-parameter α . Thus, we set α to 0.5 (*i.e.*, same importance for the two losses).

4 EXPERIMENTS AND RESULTS

In § 4.1, we first introduce the eight RGB-D datasets used in the experiments along with their training/test splits, and the five evaluation metrics. Then, we provide quantitative results and visual comparisons with SOTA methods in § 4.2. Finally, in § 4.3, we perform a detailed ablation analysis to investigate the aggregation strategies and different modules in the model.

4.1 Experimental Settings

• **Datasets.** We conduct our experiments on eight challenging RGB-D SOD benchmark datasets: NJU2K [67], NLPR [32], STERE [84], DES [35], LFSD [85], SSD [86], SIP [37] and DUT [19]. Tab. 1 provides an overview of these RGB-D datasets.

NJU2K [67] is the largest RGB-D dataset containing 1,985 image pairs. The stereo images were collected from the Internet and 3D movies, while photographs were taken by a *Fuji W3 camera*.

NLPR [32] consists of 1,000 image pairs captured by a standard *Microsoft Kinect* with a resolution of 640×480 . The images include indoor and outdoor scenes (*e.g.*, offices, campuses, streets and supermarkets).

STERE [84] is the first stereoscopic photo collection, containing 1,000 stereoscopic images downloaded from the Internet. Note that this dataset has two versions (979 vs. 1,000); here, we utilize the 1,000 images version in all experiments.

DES [35] is a small-scale RGB-D dataset that includes 135 indoor image pairs collected using a *Microsoft Kinect* with a resolution of 640×480 .

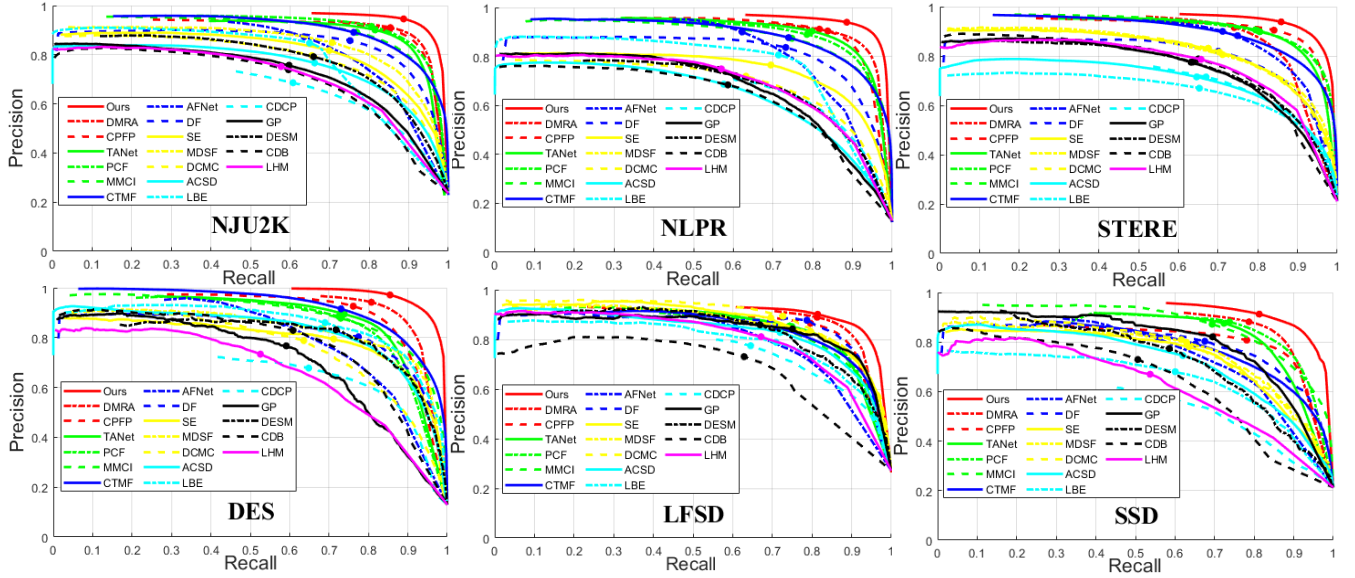


Fig. 5. **PR Curves of the proposed model and 18 SOTA algorithms over six datasets.** Dots on the curves represent the value of precision and recall at the maximum F-measure.

TABLE 1
Overview of the currently available RGB-D datasets.

#	Dataset	Size	Year	Resolution	Device	Type
1	STERE [84]	1,000	2012	[251 ~ 1,200] \times [222 ~ 900]	Internet	Indoor/outdoor
2	NJU2K [67]	1,985	2014	[231 ~ 1,213] \times [274 ~ 828]	Fuji W3 stereo camera	Internet/movies/photos
3	NLPR [32]	1,000	2014	640 \times 480, 480 \times 640	Remoulded Kinect	Indoor/outdoor
4	DES [35]	135	2014	640 \times 480	Microsoft Kinect	Indoor scene
5	LFSD [85]	80	2014	360 \times 360	Lytro light field camera	Indoor/outdoor
6	SSD [86]	80	2017	960 \times 1,080	Stere movies	Stere movies
7	DUT [19]	1,200	2019	600 \times 400	Commercial Lytro2 camera	Indoor (800)/outdoor (400)
8	SIP [37]	929	2020	744 \times 992	Huawei Mate10	Person in the wild

¹<http://web.cec.pdx.edu/~fliu/> ²<http://mcg.nju.edu.cn/publication/2014/icip14-jur/index.html>

³<https://sites.google.com/site/rgbd saliency/home> ⁴https://github.com/HZFu/DES_code

⁵<https://sites.duke.edu/nianyi/publication/saliency-detection-on-light-field/> ⁶<https://github.com/ChunbiaoZhu/TPPF>

⁷https://github.com/jiwei0921/DMRA_RGBD-SOD ⁸<http://dpfan.net/d3netbenchmark/>

LFSD [85] contains 60 image pairs from indoor scenes and 40 image pairs from outdoor scenes. The images were captured by a *Lytro light field camera* with a resolution of 360×360 .

SSD [86] includes 80 images picked from three stereo movies with both indoor and outdoor scenes. The collected images have a high resolution of $960 \times 1,080$.

SIP [37] consists of 1,000 image pairs captured by a *smart phone* with a resolution of 992×744 , using a dual camera. This dataset focuses on salient persons in real-world scenes.

DUT [19] includes multiple challenging scenes (*e.g.*, transparent objects, multiple objects, complex backgrounds and low-intensity environments). It contains 800 indoor and 400 outdoor scenes. Image pairs were captured by a *Lytro2 camera* with a resolution of 600×400 .

• Training/Testing. We follow the same settings as [19], [22] for fair comparison. In particular, the training set contains 1,485 samples from the NJU2K dataset and 700 samples from the NLPR dataset. The test set consists of the remaining images from NJU2K (500) and NLPR (300), and the

whole of STERE (1,000), DES, LFSD, SSD and SIP. As for the recent proposed DUT [19] dataset, following [19], we adopt the same training data of DUT, NJU2K, and NLPR to train the compared deep models (*i.e.*, DMRA [19], A2dele [90], SSF [91], and our *BBS-Net*) and test the performance on the test set of DUT. Please refer to Tab. 2 for more details.

• Evaluation Metrics. We employ five widely used metrics, including S-measure (S_α) [92], E-measure (E_ξ) [93], F-measure (F_β) [94], mean absolute error (MAE), and precision-recall (PR) curves to evaluate various methods.

F-measure [94] is a common evaluation metric based on the region similarity. It is defined as:

$$F_\beta^i = \frac{(1 + \beta^2)P^i \times R^i}{\beta^2 \times P^i + R^i}, \quad (13)$$

where P^i and R^i are the corresponding precision and recall for the threshold i ($i \in \{1, 2, \dots, 255\}$), respectively. β controls the trade-off between P^i and R^i . We set β^2 to 0.3, as suggested in [94]. In the experiments, we utilize the maximum F-measure (for all thresholds), the adaptive F-measure (*i.e.*, the threshold is defined as the double mean

TABLE 2

Performance of different models on the DUT [19] dataset. Models are trained and tested on the DUT using the proposed training and test sets split from [19]. A: handcrafted features-based methods. B: CNN-based methods.

#	Method	Dataset	DUT [19]		
			$S_\alpha \uparrow$	$\max F_\beta \uparrow$	$\max E_\xi \uparrow$
A	MB [95]		.607	.577	.691
	LHM [32]		.568	.659	.767
	DESM [35]		.659	.668	.733
	DCMC [96]		.499	.406	.712
	CDCP [36]		.687	.633	.794
B	DMR [19]		.888	.883	.927
	A2dele [90]		.886	.892	.929
	SSF [91]		.916	.924	.951
	BBS-Net (ours)		.920	.927	.955

TABLE 3

Speed test of *BBS-Net*. We test the speed of only predicting the initial saliency map S_1 , and the final map S_2 , respectively. ‘BS’ denotes the batch size, of which the maximum value for a single GTX 1080Ti GPU is ten. ‘io’ is the time consumed by reading and writing.

#	BS:1	BS:10	w/ io	w/o io	S_1 (fps)	S_2 (fps)
1	✓			✓	17	14
2	✓			✓	19	15
3		✓	✓		56	48
4		✓		✓	133	123

value of the saliency map) and mean F-measure (*i.e.*, the average F-measure for all thresholds) to evaluate different methods.

S-measure [92] is a structure measure which combines the region-aware structural similarity (S_r) and object-aware structural similarity (S_o). It is defined as:

$$S_\alpha = \alpha \times S_o + (1 - \alpha) \times S_r, \quad (14)$$

where $\alpha \in [0, 1]$ is a hyper-parameter to balance S_r and S_o . We set it to 0.5 as the default setting.

E-measure, recently proposed by [93], is based on cognitive vision studies and utilizes both image-level and local pixel-level statistics for evaluating the binary saliency map. It is defined as:

$$E_\xi = \frac{1}{w \times h} \sum_{x=1}^w \sum_{y=1}^h \xi(x, y), \quad (15)$$

where w and h are the width and height of the saliency map. ξ is the enhanced alignment matrix. Similar to the F-measure, we also provide the results of max E-measure, adaptive E-measure and mean E-measure.

MAE represents the average absolute error between the predicted saliency map and the ground truth. It is denoted as:

$$M = \frac{1}{N} |S - G|, \quad (16)$$

where S and G are the predicted saliency map and ground truth binary map, respectively. N represents the total number of pixels.

PR curves are generated by a series of precision-recall (PR) pairs, which are calculated by the binarized saliency

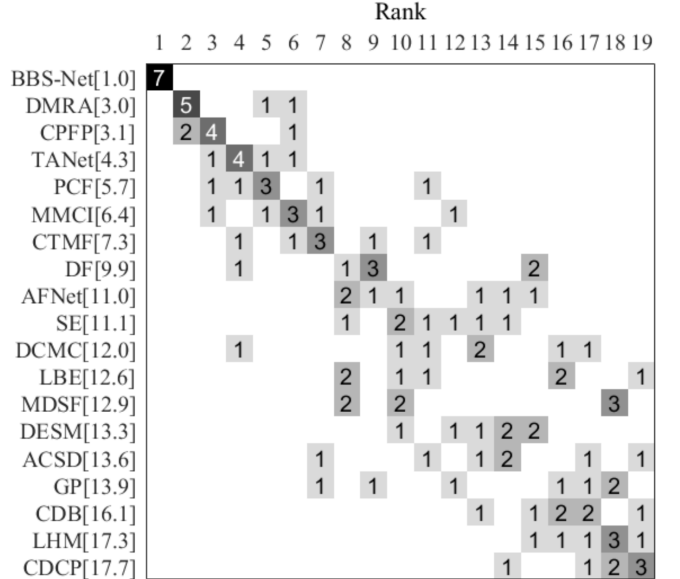


Fig. 6. Ranking of 19 models from Tab. 4 in terms of max F-measure ($\max F_\beta$). Element (i, j) represents the number of times that model i ranks j^{th} . Models are ranked by the mean rank (shown in brackets) over the seven datasets.

map with a threshold varying from 0 to 255. Specifically, the precision (P) and recall (R) are calculated as:

$$P = \frac{|S' \cap G|}{|S'|}, R = \frac{|S' \cap G|}{|G|}, \quad (17)$$

where S' is the binarized mask for the predicted map S according to the threshold.

4.2 Comparison with SOTAs

• **Contenders.** We compare the proposed *BBS-Net* with ten algorithms based on handcrafted features [28], [29], [32], [35], [36], [67], [96]–[99] and eight methods [18], [19], [21]–[23], [30], [64], [69] that use deep learning. We train and test these methods using their default settings. For the methods without released source codes, we compare with their reported results.

• **Quantitative Results.** As shown in Tab. 2, Tab. 4, and Fig. 6, our method outperforms all algorithms based on handcrafted features as well as SOTA CNN-based methods by a large margin, in terms of all four evaluation metrics (*i.e.*, S-measure (S_α), F-measure (F_β), E-measure (E_ξ) and MAE (M)). Performance gains over the best compared algorithms (ICCV’19 DMRA [19] and CVPR’19 CPFP [21]) are (2.5% ~ 3.5%, 0.7% ~ 3.9%, 0.8% ~ 2.3%, 0.009 ~ 0.016) for the metrics (S_α , $\max F_\beta$, $\max E_\xi$, M) on the seven challenging datasets. The PR curves of different methods on various datasets are shown in Fig. 5. It can be easily deduced from the PR curves that our method (*i.e.*, solid red lines) outperforms all the SOTA algorithms. In terms of speed, *BBS-Net* achieves 14 fps on a single GTX 1080Ti GPU (batch size of one), as shown in Tab. 3. When fully exploiting the single GTX 1080Ti GPU (batch size of ten),

TABLE 4

Quantitative comparison of models using S-measure (S_α), adaptive F-measure ($adpF_\beta$), mean F-measure ($meanF_\beta$), max F-measure ($maxF_\beta$), adaptive E-measure ($adpE_\xi$), mean E-measure ($meanE_\xi$), max E-measure ($maxE_\xi$) and MAE (M) scores on seven public datasets. \uparrow (\downarrow) denotes that the higher (lower) the score, the better. The best score in each row is highlighted in boldface. From left to right: ten models based on handcrafted features and eight CNNs-based models. ' S_1 ' and ' S_2 ' denote the initial and final saliency output results of the proposed method, respectively.

Dataset	Metric	Hand-crafted-features-Based Models										CNNs-Based Models								BBS-Net	
		LHM [32]	CDB [97]	DESM [35]	GP [98]	CDCP [36]	ACSD [67]	LBE [29]	DCMC [96]	MDSF [28]	SE [99]	DF [64]	AFNet [30]	CTMF [69]	MMCI [23]	PCF [22]	TANet [18]	CPFP [21]	DMRA [19]	Ours (S_1)	Ours (S_2)
NJU2K [67]	$S_\alpha \uparrow$.514	.624	.665	.527	.669	.699	.695	.686	.748	.664	.763	.772	.849	.858	.877	.878	.879	.886	.914	.921
	$adpF_\beta \uparrow$.638	.648	.632	.655	.624	.696	.740	.717	.757	.734	.804	.768	.788	.812	.844	.844	.837	.872	.889	.902
	$meanF_\beta \uparrow$.328	.482	.550	.357	.595	.512	.606	.556	.628	.583	.784	.764	.779	.793	.840	.841	.850	.873	.889	.902
	$maxF_\beta \uparrow$.632	.648	.717	.647	.621	.711	.748	.715	.775	.748	.650	.775	.845	.852	.872	.874	.877	.886	.911	.920
	$adpE_\xi \uparrow$.708	.745	.682	.716	.747	.786	.791	.791	.812	.772	.864	.846	.864	.878	.896	.893	.895	.908	.917	.924
	$meanE_\xi \uparrow$.447	.565	.590	.466	.706	.593	.655	.619	.677	.624	.835	.826	.846	.851	.895	.895	.910	.920	.930	.938
	$maxE_\xi \uparrow$.724	.742	.791	.703	.741	.803	.803	.799	.838	.813	.696	.853	.913	.915	.924	.925	.926	.927	.948	.949
NLPR [32]	$M \downarrow$.205	.203	.283	.211	.180	.202	.153	.172	.157	.169	.141	.100	.085	.079	.059	.060	.053	.051	.040	.035
	$S_\alpha \uparrow$.630	.629	.572	.654	.727	.673	.762	.724	.805	.756	.802	.799	.860	.856	.874	.886	.888	.899	.923	.930
	$adpF_\beta \uparrow$.664	.613	.563	.659	.608	.535	.736	.614	.665	.692	.744	.747	.724	.730	.795	.796	.823	.854	.867	.882
	$meanF_\beta \uparrow$.427	.422	.430	.451	.609	.429	.626	.543	.649	.624	.664	.755	.740	.737	.802	.819	.840	.864	.881	.896
	$maxF_\beta \uparrow$.622	.618	.640	.611	.645	.607	.745	.648	.793	.713	.778	.771	.825	.815	.841	.863	.867	.879	.892	.918
	$adpE_\xi \uparrow$.813	.809	.698	.804	.800	.742	.855	.786	.812	.839	.868	.884	.869	.872	.916	.916	.924	.941	.947	.952
	$meanE_\xi \uparrow$.560	.565	.541	.571	.781	.578	.719	.684	.745	.742	.755	.851	.840	.841	.887	.902	.918	.940	.942	.950
STERE [84]	$maxE_\xi \uparrow$.766	.791	.805	.723	.820	.780	.855	.793	.885	.847	.880	.879	.929	.913	.925	.941	.932	.947	.959	.961
	$M \downarrow$.108	.114	.312	.146	.112	.179	.081	.117	.095	.091	.085	.058	.056	.059	.044	.041	.036	.031	.028	.023
	$S_\alpha \uparrow$.562	.615	.642	.588	.713	.692	.660	.731	.728	.708	.757	.825	.848	.873	.875	.871	.879	.835	.899	.908
	$adpF_\beta \uparrow$.703	.713	.594	.711	.666	.661	.595	.742	.744	.748	.742	.807	.771	.829	.826	.835	.830	.844	.867	.885
	$meanF_\beta \uparrow$.378	.489	.519	.405	.638	.478	.501	.590	.527	.610	.617	.806	.758	.813	.818	.828	.841	.837	.863	.883
	$maxF_\beta \uparrow$.683	.717	.700	.671	.664	.669	.633	.740	.719	.755	.757	.823	.831	.863	.860	.861	.874	.847	.892	.903
	$adpE_\xi \uparrow$.770	.808	.675	.784	.796	.793	.749	.831	.830	.825	.838	.886	.864	.901	.897	.906	.903	.900	.918	.925
DES [35]	$meanE_\xi \uparrow$.484	.561	.579	.509	.751	.592	.601	.655	.614	.665	.691	.872	.841	.873	.887	.893	.912	.879	.917	.928
	$maxE_\xi \uparrow$.771	.823	.811	.743	.786	.806	.787	.819	.809	.846	.847	.887	.912	.927	.925	.923	.925	.911	.938	.942
	$M \downarrow$.172	.166	.295	.182	.149	.200	.250	.148	.176	.143	.141	.075	.086	.064	.060	.051	.066	.048	.041	.021
	$S_\alpha \uparrow$.578	.645	.622	.636	.709	.728	.703	.707	.741	.741	.752	.770	.863	.848	.842	.858	.872	.900	.929	.933
	$adpF_\beta \uparrow$.631	.729	.698	.686	.625	.717	.796	.702	.744	.726	.753	.730	.778	.762	.782	.795	.829	.866	.895	.906
	$meanF_\beta \uparrow$.345	.502	.483	.412	.585	.513	.576	.542	.523	.617	.604	.713	.756	.735	.765	.790	.824	.873	.896	.910
	$maxF_\beta \uparrow$.511	.723	.765	.597	.631	.756	.788	.666	.746	.741	.766	.728	.844	.822	.804	.827	.846	.888	.919	.927
LFSD [85]	$adpE_\xi \uparrow$.761	.868	.759	.785	.816	.855	.911	.849	.869	.852	.877	.874	.911	.904	.912	.919	.927	.944	.966	.967
	$meanE_\xi \uparrow$.477	.572	.565	.503	.748	.612	.649	.632	.621	.707	.684	.810	.826	.825	.838	.863	.889	.933	.940	.949
	$maxE_\xi \uparrow$.653	.830	.868	.670	.811	.850	.890	.773	.851	.856	.870	.881	.932	.928	.893	.910	.923	.943	.945	.966
	$M \downarrow$.114	.100	.299	.168	.115	.169	.208	.111	.122	.090	.093	.068	.055	.065	.049	.046	.038	.030	.024	.021
	$S_\alpha \uparrow$.553	.515	.716	.635	.712	.727	.729	.753	.694	.692	.783	.738	.788	.787	.786	.801	.828	.839	.859	.864
	$adpF_\beta \uparrow$.714	.678	.676	.752	.695	.751	.705	.812	.795	.774	.802	.738	.778	.775	.788	.790	.809	.845	.850	.858
	$meanF_\beta \uparrow$.395	.374	.611	.516	.679	.562	.610	.652	.518	.636	.676	.732	.752	.718	.757	.767	.807	.841	.828	.843
SSD [86]	$maxF_\beta \uparrow$.708	.677	.762	.783	.702	.763	.722	.817	.779	.786	.813	.744	.787	.771	.775	.796	.826	.852	.854	.858
	$adpE_\xi \uparrow$.730	.696	.701	.776	.773	.794	.763	.835	.831	.800	.836	.802	.844	.832	.838	.838	.859	.892	.886	.889
	$meanE_\xi \uparrow$.488	.461	.632	.580	.748	.620	.664	.677	.583	.648	.719	.788	.802	.767	.810	.813	.856	.885	.871	.883
	$maxE_\xi \uparrow$.763	.871	.811	.824	.780	.829	.797	.856	.819	.832	.857	.815	.857	.839	.827	.847	.863	.893	.896	.901
	$M \downarrow$.218	.225	.253	.190	.172	.195	.214	.155	.197	.174	.145	.133	.127	.132	.119	.111	.088	.083	.079	.072
	$S_\alpha \uparrow$.566	.562	.602	.615	.603	.675	.621	.704	.673	.675	.747	.714	.776	.813	.841	.839	.807	.857	.878	.882
	$adpF_\beta \uparrow$.580	.628	.614	.749	.522	.656	.613	.679	.674	.693	.724	.694	.710	.748	.791	.767	.726	.821	.829	.849
SIP [37]	$meanF_\beta \uparrow$.367	.347	.502	.453	.515	.469	.489	.572	.470	.564	.624	.672	.689	.721	.777	.773	.747	.828	.829	.843
	$maxF_\beta \uparrow$.568	.592	.680	.740	.535	.682	.619	.711	.703	.710	.735	.687	.729	.781	.807	.810	.766	.844	.853	.859
	$adpE_\xi \uparrow$.730	.737	.683	.795	.705	.765	.729	.786	.772	.778	.812	.803	.838	.860	.886	.879	.832	.903	.912	.912
	$meanE_\xi \uparrow$.498	.477	.560	.529	.676	.566	.574	.646	.576	.631	.690	.762	.796	.856	.861	.839	.897	.894	.904	.904
	$maxE_\xi \uparrow$.717	.698	.769	.782	.700	.785	.736	.786	.779	.800	.828	.807	.865	.882	.894	.897	.852	.906	.922	.919
	$M \downarrow$.195	.196	.308	.180	.214	.203	.278	.169	.192	.165	.142	.118	.099	.082	.062	.063	.082	.058	.050	.044
	$S_\alpha \uparrow$.511	.557	.616	.588	.595	.732	.727	.683	.717	.628	.653	.720	.716	.833	.842	.835	.850	.806	.875	.879
CPFP [21]	$adpF_\beta \uparrow$.592	.624	.644	.699	.495	.727	.733	.645	.694	.662	.673	.705	.684	.795	.825	.809	.819	.862	.872	.872
	$meanF_\beta \uparrow$.287	.341	.496	.411	.482	.542	.571	.499	.568	.515	.464	.702	.608	.771	.814	.803	.821	.811	.855	.868
	$maxF_\beta \uparrow$.574	.620	.669	.687	.505	.763	.751	.618	.698	.661	.657	.712	.694	.818	.838	.830	.851	.821	.877	.883
	$adpE_\xi \uparrow$.719</td																			

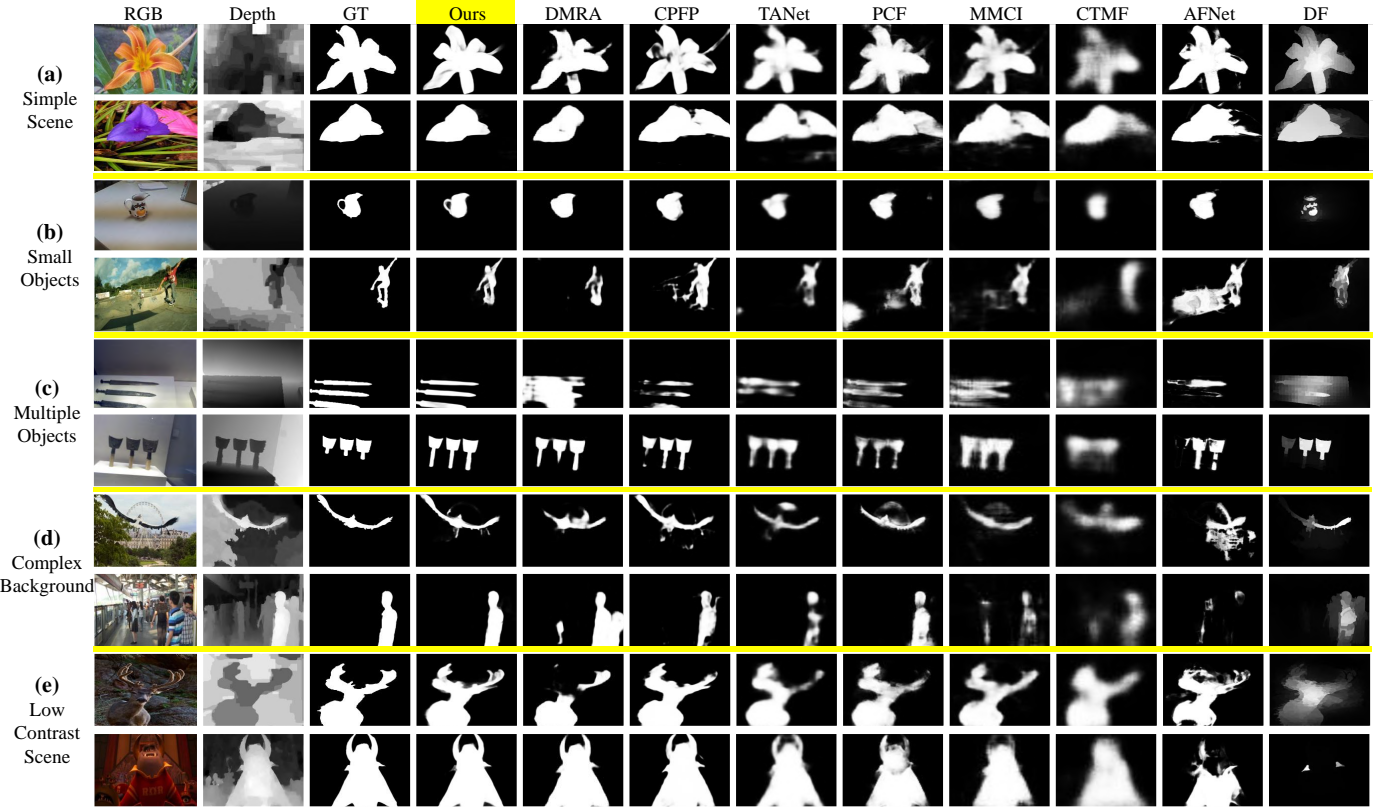


Fig. 7. **Qualitative visual comparison of our model versus eight SOTA models.** Unlike other models, our method not only locates the salient object accurately, but it also produces sharper edges with fewer background distractors in various scenarios, including simple scenes (a), small objects (b), multiple objects (c), complex backgrounds (d), and low contrast scenes (e).

TABLE 5
Performance comparison using different backbone models. We experiment with multiple popular backbone models used in RGB-D SOD, including VGG-16 [100], VGG-19 [100] and ResNet-50 [68].

Models	NJU2K [67] $S_\alpha \uparrow$ $M \downarrow$		NLPR [32] $S_\alpha \uparrow$ $M \downarrow$		STERE [84] $S_\alpha \uparrow$ $M \downarrow$		DES [35] $S_\alpha \uparrow$ $M \downarrow$		LFSD [85] $S_\alpha \uparrow$ $M \downarrow$		SSD [86] $S_\alpha \uparrow$ $M \downarrow$		SIP [37] $S_\alpha \uparrow$ $M \downarrow$	
TANet (VGG-16) [18]	.878	.060	.886	.041	.871	.060	.858	.046	.801	.111	.839	.063	.835	.075
CPFP (VGG-16) [21]	.879	.053	.888	.036	.879	.051	.872	.038	.828	.088	.807	.082	.850	.064
Ours (VGG-16)	.916	.039	.923	.026	.896	.046	.908	.028	.845	.080	.858	.055	.874	.056
DMRA (VGG-19) [19]	.886	.051	.899	.031	.835	.066	.900	.030	.839	.083	.857	.058	.806	.085
Ours (VGG-19)	.918	.037	.925	.025	.901	.043	.915	.026	.852	.074	.855	.056	.878	.054
D3Net (ResNet-50) [37]	.900	.041	.912	.030	.899	.046	.898	.031	.825	.095	.857	.058	.860	.063
Ours (ResNet-50)	.921	.035	.930	.023	.908	.041	.933	.021	.864	.072	.882	.044	.879	.055

• **Visual Comparison.** Fig. 7 provides examples of maps predicted by our method and several SOTA algorithms. Visualizations cover simple scenes (a) and various challenging scenarios, including small objects (b), multiple objects (c), complex backgrounds (d), and low contrast scenes (e).

First, the first row of (a) shows an easy example. The flower in the foreground is evident in the original RGB image, but the depth map is of low quality and contains some misleading information. The SOTA algorithms, such as DMRA and CPFP, fail to predict the whole extent of the salient object due to the interference from the depth map. Our method can eliminate the side-effects of the depth map by utilizing the complementary depth information more effectively. Second, two examples of small objects are shown in (b). Despite the handle of the teapot in the first row being tiny, our method can accurately detect it. Third, we show

two examples with multiple objects in an image in (c). Our method locates all salient objects in the image. It segments the objects more accurately and generates sharper edges compared to other algorithms. Even though the depth map in the first row of (c) lacks clear information, our algorithm predicts the salient objects correctly. Fourth, (d) shows two examples with complex backgrounds. Here, our method produces reliable results, while other algorithms confuse the background as a salient object. Finally, (e) presents two examples in which the contrast between the object and the background is low. Many algorithms fail to detect and segment the entire extent of the salient object. Our method produces satisfactory results by suppressing background distractors and exploring the informative cues from the depth map.

TABLE 6

Comparison of different feature aggregation strategies on seven datasets. 1: Only aggregating the low-level features ($Conv1 \sim 3$), 2: Only aggregating the high-level features ($Conv3 \sim 5$), 3: Directly integrating all five-level features ($Conv1 \sim 5$) by a single decoder, 4: Our model without the refinement flow, 5: High-level features ($Conv3 \sim 5$) are first refined by the initial map aggregated by low-level features ($Conv1 \sim 3$) and are then integrated to generate the final saliency map, and 6: The proposed cascaded refinement mechanism.

#	Settings	NJU2K [67]		NLPR [32]		STERE [84]		DES [35]		LFSD [85]		SSD [86]		SIP [37]	
		$S_\alpha \uparrow$	$M \downarrow$												
1	Low 3 levels	.881	.051	.882	.038	.832	.070	.853	.044	.779	.110	.805	.080	.760	.108
2	High 3 levels	.902	.042	.911	.029	.886	.048	.912	.026	.845	.080	.850	.058	.833	.073
3	All 5 levels	.905	.042	.915	.027	.891	.045	.901	.028	.845	.082	.848	.060	.839	.071
4	BBS-NoRF	.893	.050	.904	.035	.843	.072	.886	.039	.804	.105	.839	.069	.843	.076
5	BBS-RH	.913	.040	.922	.028	.881	.054	.919	.027	.833	.085	.872	.053	.866	.063
6	BBS-RL (ours)	.921	.035	.930	.023	.908	.041	.933	.021	.864	.072	.882	.044	.879	.055

TABLE 7

Ablation analysis of our *BBS-Net* on different datasets. ‘BM’ denotes the base model. ‘CA’ and ‘SA’ represent the channel attention and spatial attention mechanisms of the depth-enhanced module, respectively. ‘PTM’ is the progressively transposed module.

#	BM	Settings	CA	SA	PTM	NJU2K [67]	NLPR [32]	STERE [84]	DES [35]	LFSD [85]	SSD [86]	SIP [37]							
						$S_\alpha \uparrow$	$M \downarrow$												
1	✓					.908	.045	.918	.029	.882	.055	.917	.027	.842	.083	.862	.057	.864	.066
2	✓	✓				.913	.042	.922	.027	.896	.048	.923	.025	.840	.086	.855	.057	.868	.063
3	✓		✓			.912	.045	.918	.029	.891	.054	.914	.029	.855	.083	.872	.054	.869	.063
4	✓	✓	✓			.919	.037	.928	.026	.900	.045	.924	.024	.861	.074	.873	.052	.869	.061
5	✓	✓	✓	✓	✓	.921	.035	.930	.023	.908	.041	.933	.021	.864	.072	.882	.044	.879	.055

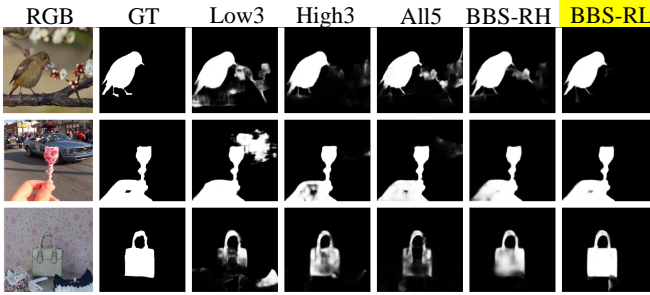


Fig. 8. **Visual comparison of different aggregation strategies.** ‘Low3’ only integrates low-level features ($Conv1 \sim 3$), while ‘High3’ aggregates high-level features ($Conv3 \sim 5$) for predicting the saliency map. ‘All5’ combines all five-level features directly for prediction. ‘BBS-RH/BBS-RL’ denotes that high-level/low-level features are first refined by the initial map aggregated by the low-level/high-level features and are then integrated to predict the final map.

4.3 Ablation Study

• **Analysis of Different Aggregation Strategies.** To validate the effectiveness of our cascaded refinement mechanism, we conduct several experiments to explore different aggregation strategies. Results are shown in Tab. 6 and Fig. 8. ‘Low3’ means that we only integrate the low-level features ($Conv1 \sim 3$) using the decoder without the refinement from the initial map. Low-level features contain abundant details that are beneficial for refining the object edges, but at the same time introduce a lot of background distraction. Integrating only low-level features produces inadequate results and generates many distractors (e.g., the first and second rows in Fig. 8) or fails to locate the salient objects (e.g., the third row in Fig. 8). ‘High3’ only integrates the high-level features ($Conv3 \sim 5$) to predict the saliency map.

TABLE 8
Effectiveness analysis of the cascaded decoder in terms of the S-measure (S_α) on seven datasets.

Methods	NJU2K [67]	NLPR [32]	STERE [84]	DES [35]	SSD [86]	LFSD [85]	SIP [37]
Element-wise sum	.915	.925	.897	.925	.868	.856	.880
Cascaded decoder	.921	.930	.908	.933	.882	.864	.879

Compared with low-level features, high-level features contain more semantic information. As a result, they help locate the salient objects and preserve edge information. Thus, integrating high-level features leads to better results. ‘All5’ aggregates features from all five levels ($Conv1 \sim 5$) directly, using a single decoder for training and testing. It achieves comparable results with the ‘High3’ but may include background noise introduced by the low-level features (see column ‘All5’ in Fig. 8). ‘BBS-NoRF’ indicates that we directly remove the refinement flow of our model. This leads to poor performance. ‘BBS-RH’ is a reverse refinement strategy to our cascaded refinement mechanism, where teacher features ($Conv3 \sim 5$) are first refined by the initial map aggregated by low-level features ($Conv1 \sim 3$) and are then integrated to generate the final saliency map. It performs worse than the proposed mechanism (BBS-RL), because noise in low-level features cannot be effectively suppressed in this reverse refinement strategy. Besides, compared to ‘All5’, our method fully utilizes the features at different levels, and thus achieves significant performance improvement (i.e., the last row in Tab. 6) with fewer background distractors and sharper edges (i.e., the last column in Fig. 8).

• **Impact of Different Modules.** To validate the effectiveness of the different modules in the proposed *BBS-Net*, we conduct various experiments, as shown in Tab. 7 and Fig.

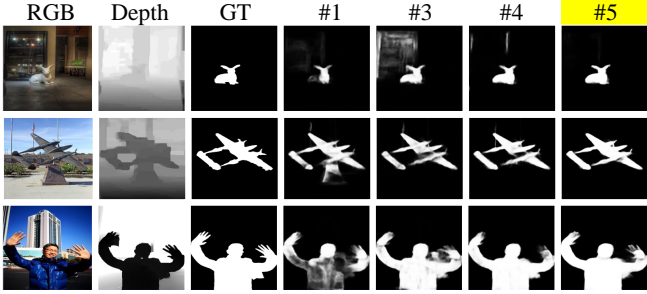


Fig. 9. **Analysis of gradually adding various modules.** The first three columns are the RGB, depth, and ground-truth images, respectively. ‘#’ denotes the corresponding row of Tab. 7.

9. The base model (BM) is our *BBS-Net* without additional modules (*i.e.*, CA, SA, and PTM). Note that the BM alone performs better than the SOTA methods over almost all datasets, as shown in Tab. 4 and Tab. 7. Adding the channel attention (CA) and spatial attention (SA) modules enhances the performance on most of the datasets (see the results shown in the second and third rows of Tab. 7). When we combine the two modules (the fourth row in Tab. 7), the performance is greatly improved on all datasets, compared to the BM. We can easily conclude from the ‘#3’ and ‘#4’ columns in Fig. 9 that the spatial attention and channel attention mechanisms in DEM allow the model to focus on the informative parts of the depth features, which results in better suppression of background clutter. Finally, we add a progressively transposed block before the second decoder to gradually upsample the feature map to the same resolution as the ground truth. The results in the fifth row of Tab. 7 and the ‘#5’ column of Fig. 9 show that the ‘PTM’ achieves impressive performance gains on all datasets and generates sharper edges with finer details.

To further analyze the effectiveness of the cascaded decoder, we experiment with changing it to an element-wise summation mechanism. That is to say, we first change the features from different layers to the same dimension using 1×1 convolution and upsampling operation and then fuse them by element-wise summation. Experimental results in Tab. 8 show that the cascaded decoder achieves comparable results on SIP, and outperforms the element-wise sum on the other six datasets, which demonstrates its effectiveness.

5 DISCUSSION

In this section, we discuss four aspects pertaining to our model. In § 5.1, we provide an analysis of the failure cases produced by our model. Then, we discuss the benefits of the depth information for SOD in § 5.2. Further, we investigate the effects of different post-processing methods in § 5.3. Finally, in § 5.4, to provide a qualitative evaluation of different RGB-D datasets, we discuss the cross-dataset generalization ability of the widely used RGB-D datasets.

5.1 Failure Case Analysis

We illustrate six representative failure cases in Fig. 10. The failure examples are divided into four categories. In the first category, the model either misses the salient object or detects

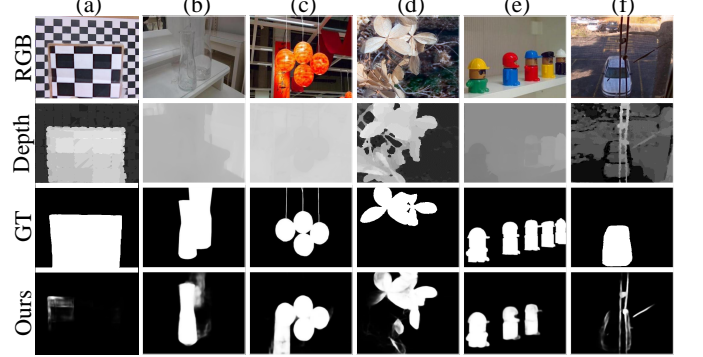


Fig. 10. Some representative failure cases of the model.

it imperfectly. For example, in column (a), our model fails to detect the salient object even when the depth map has clear boundaries. This is because the salient object has the same texture and content layout as the background in the RGB image. Thus, the model cannot find the salient object based only on the borders. In column (b), our method cannot fully segment the transparent salient objects, since the background has low contrast, and depth map lacks useful information. The second situation is that the model identifies the background as the salient part. For example, the lanterns in column (c) have a similar color to the background wallpaper, which confuses the model into thinking that the wallpaper is the salient object. Besides, the background of the RGB image in column (d) is complex and thus our model does not detect the complete salient objects. The third type of failure case is when an image contains several separate salient objects. In this case, our model may not detect them all. As shown in column (e), with five salient objects in the RGB images, the model fails to detect the two objects that are far from the camera. This may be because the model tends to consider the objects that are closer to the camera more salient. The final case is when salient objects are occluded by non-salient ones. Note that in column (f), the car is occluded by two ropes in front of the camera. Here our model predicts the ropes as salient objects.

Most of these failure cases can be attributed to interference information from the background (*e.g.*, color, contrast, and content). We propose some ideas that may be useful for solving these failure cases. The first is to introduce some human-designed prior knowledge, such as providing a boundary that can approximately distinguish the foreground from the background. Leveraging such prior knowledge, the model may better capture the characteristics of the background and salient objects. This strategy may contribute significantly to solving the failure cases especially for columns (a) and (b). Besides, the depth map can also be seen as a type of prior knowledge for this task. Thus, some failure cases (*i.e.*, (b), (c) and (e)) may be solved when a high-quality depth map is available. Second, we find that in the current RGB-D datasets, the image pairs for challenging scenarios (*e.g.*, complex backgrounds, low-contrast backgrounds, transparent objects, multiple objects, shielded objects, and small objects) constitute a small fraction of the whole dataset. Therefore, adding more difficult examples to the training data could help mitigate the failure cases.

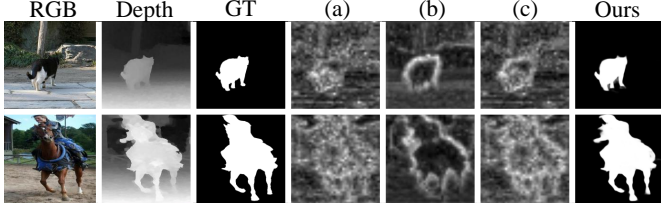


Fig. 11. Feature visualization. Here, (a), (b), and (c) are the average RGB feature, depth feature and cross-modal feature of the *Conv3* layer. To visualize them, we average the feature maps along their channel axis to obtain the visualization map. ‘Ours’ refers to the BBS-Net (w/ depth).

TABLE 9

S-measure (S_α) comparison with SOTA RGB SOD methods on seven datasets. ‘w/o depth’ and ‘w/ depth’ represent training and testing the proposed method without/with the depth information (*i.e.*, the inputs of the depth branch are or are not set to zeros).

Methods	NJU2K [67]	NLPR [32]	STERE [84]	DES [35]	LFSD [85]	SSD [86]	SIP [37]
PiCANet [101]	.847	.834	.868	.854	.761	.832	-
PAGRN [48]	.829	.844	.851	.858	.779	.793	-
R3Net [81]	.837	.798	.855	.847	.797	.815	-
CPD [27]	.894	.915	.902	.897	.815	.839	.859
PoolNet [16]	.887	.900	.880	.873	.787	.773	.861
BBS-Net (w/o depth)	.914	.925	.915	.912	.836	.855	.875
BBS-Net (w/ depth)	.921	.930	.908	.933	.864	.882	.879

Finally, depth maps may sometimes introduce misleading information, such as in column (d). Considering how to exploit salient cues from the RGB image to suppress the noise in the depth map could be a promising solution.

5.2 Utility of Depth Information

To explore whether depth information can really contribute to the performance of SOD, we conduct two experiments, results of which are shown in Tab. 9. On the one hand, we compare the proposed method with five SOTA RGB SOD methods (*i.e.*, PiCANet [101], PAGRN [48], R3Net [81], CPD [27], and PoolNet [16]) by neglecting the depth information. We train and test CPD and PoolNet using the same training and test sets as our model. For other methods, we use the published results from [19]. It is clear that the proposed methods (*i.e.*, BBS-Net (w/ depth)) can significantly exceed SOTA RGB SOD methods thanks to depth information. On the other hand, we train and test the proposed method without using the depth information by setting the inputs of the depth branch to zero (*i.e.*, BBS-Net (w/o depth)). Comparing the results of the last two rows in the table, we find that depth information effectively improves the performance of the proposed model (especially over the small datasets, *i.e.*, DES, LFSD, and SSD).

The two experiments together demonstrate the benefits of the depth information for SOD. Depth map serves as prior knowledge and provides spatial distance information and contour guidance to detect salient objects. For example, in Fig. 11, depth feature (b) has high activation on the object border. Thus, cross-modal feature (c) has clearer borders compared with the original RGB feature (a).

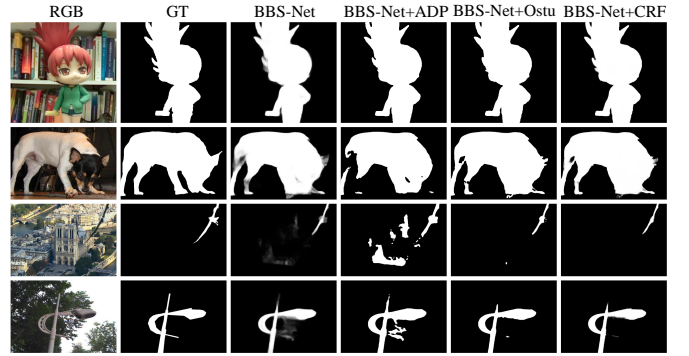


Fig. 12. Visual effects of different post-processing methods. We explore three methods, including the adaptive threshold cut (‘ADP’ in the paper), Ostu’s method and the popular algorithm of conditional random fields (CRF).

5.3 Analysis of Post-processing Methods

According to [102]–[104], the predicted saliency maps can be further refined by post-processing methods. This may be useful to sharpen the salient edges and suppress the background response. We conduct several experiments to study the effects of various post-processing methods, including the adaptive threshold cut (*i.e.*, the threshold is defined as the double of the mean value of the saliency map), Ostu’s method [105], and conditional random field (CRF) [106]. The performance comparisons of the post-processing methods in terms of MAE are shown in Tab. 12, while a visual comparison is provided in Fig. 12.

From the results, we draw the following conclusions. First, the three post-processing methods all make the salient edges sharper, as shown in the fourth to sixth columns in Fig. 12. Second, both Ostu and CRF help reduce the MAE effectively, as shown in Tab. 12. This is possibly because they can suppress the background noise. As shown in the third and fourth rows of Fig. 12, Ostu and CRF can significantly reduce the background noise, while the adaptive threshold operation further expands the background blur from the original results of BBS-Net. Further, the three post-processing methods perform similarly when the original saliency map is of high quality (*i.e.*, the first row in Fig. 12). They behave differently, however, when the predicted map is of low quality (*i.e.*, the second to fourth rows in Fig. 12). In terms of overall results, CRF performs the best, while the adaptive threshold algorithm is the worst. Ostu performs worse than CRF, because it cannot always fully eliminate the background noise (*e.g.*, the fifth and sixth columns in Fig. 12).

5.4 Cross-Dataset Generalization Analysis

For a deep model to obtain reasonable performance in real-world scenarios, it not only requires an efficient design but must also be trained on a high-quality dataset with a great generalization power. A good dataset usually contains sufficient images, with all types of variations that occur in reality, so that deep models trained on it can generalize well to the real world. In the area of RGB-D SOD, there are several large-scale datasets (*i.e.*, NJU2K, NLPR, STERE, SIP, and DUT), with around 1,000 training images.

TABLE 10

Performance comparison when training with different datasets (*i.e.*, NJU2K [67], NLPR [32], STERE [84], SIP [37] and DUT [19]). The number in parentheses denotes the number of the corresponding training and test images. ‘Self’ indicates training and testing on the same dataset. ‘Mean Others’ represents the average performance on all test sets except ‘self’. ‘Drop’ means the (percent) drop from ‘Self’ to ‘Mean Others’.

Train \ Test	NJU2K (585)		NLPR (300)		STERE (300)		SIP (229)		DUT (400)		Self		Mean Others		Drop ↓	
Train	$S_\alpha \uparrow$	$F_\beta \uparrow$														
NJU2K (1,400)	.920	.921	.840	.797	.877	.858	.805	.788	.750	.721	.920	.921	.818	.791	11%	14%
NLPR (700)	.731	.718	.919	.907	.881	.882	.880	.875	.787	.789	.919	.907	.820	.816	11%	10%
STERE (700)	.819	.800	.875	.845	.901	.891	.900	.902	.779	.768	.901	.891	.843	.829	6%	8%
SIP (700)	.457	.369	.649	.532	.562	.651	.957	.966	.457	.372	.957	.966	.531	.481	44%	50%
DUT (800)	.827	.825	.861	.821	.846	.835	.860	.865	.912	.918	.912	.918	.849	.837	7%	9%
Mean Others	.709	.678	.806	.749	.792	.807	.861	.858	.693	.663	-	-	-	-	-	-

TABLE 11

Performance comparison when training with different combinations of multiple datasets (*i.e.*, NJU2K [67], NLPR [32], STERE [84] and SIP [37]). ‘NJ’, ‘NL’, ‘ST’, ‘SI’ and ‘DU’ represent NJU2K, NLPR, STERE, SIP and DUT, respectively. The number in parentheses denotes the number of corresponding training and test images. The number of training images for each dataset is: NJ (1,400), NL (700), ST (700), SI (700), and DU (800). The row in gray shading represents the proposed training set. The corresponding training and test sets will be available at:

<https://drive.google.com/open?id=13bDyXibmryiwFtcm0xgmtlOpq1GVnXUM>.

Train \ Test	NJ (585)	NL (300)	ST (300)	DES (135)	LFSD (80)	SSD (80)	SI (229)	DU (400)	
Train	$S_\alpha \uparrow F_\beta \uparrow M \downarrow$								
NJ+NL (2,100)	.920	.919	.037	.930	.920	.025	.904	.900	.041
NJ+ST (2,100)	.922	.923	.034	.873	.843	.046	.922	.918	.032
NJ+DU (2,200)	.921	.923	.035	.860	.823	.049	.889	.878	.047
NL+ST (1,400)	.773	.739	.109	.924	.913	.028	.913	.911	.038
NL+DU (1,500)	.799	.794	.092	.923	.913	.028	.890	.890	.048
ST+DU (1,500)	.821	.803	.081	.898	.882	.035	.915	.910	.035
NJ+NL+ST (2,800)	.921	.921	.035	.929	.918	.027	.924	.925	.032
NJ+NL+DU (2,900)	.921	.924	.035	.926	.915	.026	.898	.891	.046
NJ+ST+DU (2,900)	.923	.925	.035	.895	.874	.035	.919	.914	.034
NL+ST+DU (2,200)	.829	.820	.078	.929	.918	.025	.920	.919	.034
NJ+NL+ST+DU (3,600)	.923	.926	.034	.928	.916	.028	.923	.921	.032

TABLE 12

Performance comparison (MAE) of different post-processing strategies on seven datasets. The post-processing methods include the adaptive threshold cut algorithm (ADP), Ostu algorithm and conditional random fields (CRF). The row in gray shading represents the best method.

Strategy	NJU2K [67]	NLPR [32]	STERE [84]	DES [35]	LFSD [85]	SSD [86]	SIP [37]
BBS-Net	.035	.023	.041	.021	.072	.044	.055
BBS-Net+ADP	.050	.024	.049	.018	.072	.053	.055
BBS-Net+Ostu	.030	.020	.036	.018	.066	.039	.051
BBS-Net+CRF	.030	.020	.035	.019	.065	.038	.051

• **Single Dataset Generalization Analysis.** Here, we conduct cross-dataset generalization experiments on five datasets to measure their generalization ability. Following common split ratio strategies (*e.g.*, CPFP [21], DMRA [19], and UC-Net [70]), we create new training and test splits for NJU2K, NLPR, STERE, and SIP to carry out the experiments. For NJU2K, we randomly select 1,400 image pairs for training and the remaining 585 images are used for testing. For NLPR, STERE, and SIP, we randomly choose 700 image pairs for training and the rest are used for testing. As for DUT, we maintain the original training-test split (*i.e.*, 800 images for training and 400 images for testing) proposed by [19]. We then retrain the proposed model on a single training set, and test it on all four test sets.

The results are summarized in Tab. 10. ‘Self’ represents

the results of training and testing on the same dataset. ‘Mean Others’ indicates the average performance on all test sets except self. ‘Drop’ means the (percent) drop from ‘Self’ to ‘Mean Others’. First, it can be seen from the table that DUT is the hardest dataset, since its ‘Mean Others’ of column ‘DUT’ is the lowest among the five datasets. This is because DUT includes multiple challenging scenes (*e.g.*, transparent objects, multiple objects, complex backgrounds, *etc*). Second, STERE has the best generalization ability, because the drop is lowest among all five datasets. Besides, SIP generalizes worst (*i.e.*, the drop is the largest among all five datasets), since it mainly focuses on a single person or multiple persons in the wild. We also notice that the score of the SIP column (‘Mean Others’) is the highest. This is likely because the quality of the depth maps captured by the Huawei Mate10 is higher than that produced by the traditional devices. Finally, none of the models trained with a single dataset perform best over all test sets. Thus, we further explore training on different combinations of datasets with the aim of building a dataset with a strong generalization ability for future research.

• **Dataset Combination for Generalization Improvement.** According to the results in Tab. 10, the model trained on the SIP dataset does not generalize well to other datasets, so we discard it. We thus select four relatively large-scale datasets, *i.e.*, NJU2K, NLPR, STERE, and DUT, to conduct our multi-dataset training experiments. As shown in Tab.

11, we consider all possible training combinations of these four datasets and test the models on all available test sets.

From the results in the table, we draw the following conclusions. First, more training examples do not necessarily lead to better performance on some test sets. For example, although 'NJ+NL+ST', 'NJ+NL+DU' and 'NJ+NL+ST+DU' contain external training sets, unlike 'NJ+NL', they perform similarly with 'NJ+NL' on the test set of 'NL'. Second, including the NJU2K dataset is important for the model to generalize well to small datasets (*i.e.*, LFSD, SSD). The model trained using the combinations without NJU2K (*i.e.*, 'NL+ST' 'NL+DU', 'ST+DU' and 'NL+ST+DU') all obtain low F-measure values (less than 0.8) on the LFSD and SSD test sets. In contrast, including 'NL' in the training sets increases the F-measures on the LFSD and SSD datasets by over 0.05. Finally, including more examples in the training sets can improve the stability of the model, as it allows diverse scenarios to be taken into consideration. Thus, the model trained on 'NJ+NL+ST+DU', which has the most examples, obtains the best, or are very close to the best, performance. Due to the limited size of current RGB-D datasets, it is hard for a model trained using a single dataset to perform well under various scenarios. Thus, we recommend training a model using a combination of datasets with diverse examples to avoid model over-fitting issues. To promote the development of RGB-D SOD, we hope more challenging RGB-D datasets with diverse examples and high-quality depth maps can be proposed in the future.

6 CONCLUSION

In this paper, we present a Bifurcated Backbone Strategy Network (*BBS-Net*) for the RGB-D SOD. To effectively suppress the intrinsic distractors in low-level cross-modal features, we propose to leverage the characteristics of multi-level cross-modal features in a cascaded refinement way: *low-level features are refined by the initial saliency map that is produced by the high-level cross-modal features*. Besides, we introduce a depth-enhanced module to excavate the informative cues from the depth features in the channel and spatial views, in order to improve the cross-modal compatibility when merging RGB and depth features. Experiments on eight challenging datasets demonstrate that *BBS-Net* outperforms 18 SOTA models, by a large margin, under multiple evaluation metrics. Finally, we conduct a comprehensive analysis of the existing RGB-D datasets and propose a powerful training set with a strong generalization ability for future research.

REFERENCES

- [1] D.-P. Fan, Y. Zhai, A. Borji, J. Yang, and L. Shao, "BBS-Net: RGB-D Salient Object Detection with a Bifurcated Backbone Strategy Network," in *European Conference on Computer Vision*, 2020.
- [2] A. Borji, M.-M. Cheng, H. Jiang, and J. Li, "Salient object detection: A benchmark," *IEEE Transactions on Image Processing*, vol. 24, no. 12, pp. 5706–5722, 2015.
- [3] W. Wang, Q. Lai, H. Fu, J. Shen, H. Ling, and R. Yang, "Salient object detection in the deep learning era: An in-depth survey," *arXiv preprint arXiv:1904.09146*, 2019.
- [4] M.-M. Cheng, Y. Liu, W. Lin, Z. Zhang, P. L. Rosin, and P. H. S. Torr, "BING: binarized normed gradients for objectness estimation at 300fps," *Computational Visual Media*, vol. 5, no. 1, pp. 3–20, 2019.
- [5] M.-M. Cheng, Q. Hou, S. Zhang, and P. L. Rosin, "Intelligent visual media processing: When graphics meets vision," *Journal of Computer Science and Technology*, vol. 32, no. 1, pp. 110–121, 2017.
- [6] W. Wang, J. Shen, R. Yang, and F. Porikli, "Saliency-aware video object segmentation," *IEEE Transactions on Pattern Analysis and Machine Intelligence*, vol. 40, no. 1, pp. 20–33, 2017.
- [7] M.-M. Cheng, F.-L. Zhang, N. J. Mitra, X. Huang, and S.-M. Hu, "Repfinder: Finding approximately repeated scene elements for image editing," *ACM Transactions on Graphics*, vol. 29, no. 4, pp. 83:1–83:8, 2010.
- [8] D.-P. Fan, W. Wang, M.-M. Cheng, and J. Shen, "Shifting more attention to video salient object detection," in *The IEEE Conference on Computer Vision and Pattern Recognition*, 2019, pp. 8554–8564.
- [9] P. Yan, G. Li, Y. Xie, Z. Li, C. Wang, T. Chen, and L. Lin, "Semi-supervised video salient object detection using pseudo-labels," in *The IEEE International Conference on Computer Vision*, 2019, pp. 7284–7293.
- [10] A. Borji, S. Frintrop, D. N. Sihite, and L. Itti, "Adaptive object tracking by learning background context," in *The IEEE Conference on Computer Vision and Pattern Recognition Workshops*, 2012, pp. 23–30.
- [11] S. Hong, T. You, S. Kwak, and B. Han, "Online tracking by learning discriminative saliency map with convolutional neural network," in *International Conference on Machine Learning*, 2015, pp. 597–606.
- [12] M.-M. Cheng, N. J. Mitra, X. Huang, P. H. S. Torr, and S.-M. Hu, "Global contrast based salient region detection," *IEEE Transactions on Pattern Analysis and Machine Intelligence*, vol. 37, no. 3, pp. 569–582, 2015.
- [13] D. Zhang, D. Meng, and J. Han, "Co-saliency detection via a self-paced multiple-instance learning framework," *IEEE Transactions on Pattern Analysis and Machine Intelligence*, vol. 39, no. 5, pp. 865–878, 2016.
- [14] A. Borji and L. Itti, "State-of-the-art in visual attention modeling," *IEEE Transactions on Pattern Analysis and Machine Intelligence*, vol. 35, no. 1, pp. 185–207, 2012.
- [15] A. Borji, "Saliency prediction in the deep learning era: Successes and limitations," *IEEE Transactions on Pattern Analysis and Machine Intelligence*, 2019.
- [16] J.-J. Liu, Q. Hou, M.-M. Cheng, J. Feng, and J. Jiang, "A simple pooling-based design for real-time salient object detection," in *The IEEE Conference on Computer Vision and Pattern Recognition*, 2019, pp. 3917–3926.
- [17] L. Wang, L. Wang, H. Lu, P. Zhang, and X. Ruan, "Salient object detection with recurrent fully convolutional networks," *IEEE Transactions on Pattern Analysis and Machine Intelligence*, vol. 41, no. 7, pp. 1734–1746, 2018.
- [18] H. Chen and Y. Li, "Three-stream attention-aware network for RGB-D salient object detection," *IEEE Transactions on Image Processing*, vol. 28, no. 6, pp. 2825–2835, 2019.
- [19] Y. Piao, W. Ji, J. Li, M. Zhang, and H. Lu, "Depth-induced multi-scale recurrent attention network for saliency detection," in *The IEEE International Conference on Computer Vision*, 2019, pp. 7254–7263.
- [20] N. Li, J. Ye, Y. Ji, H. Ling, and J. Yu, "Saliency detection on light field," *IEEE Transactions on Pattern Analysis and Machine Intelligence*, vol. 39, no. 8, pp. 1605–1616, 2016.
- [21] J.-X. Zhao, Y. Cao, D.-P. Fan, M.-M. Cheng, X.-Y. Li, and L. Zhang, "Contrast prior and fluid pyramid integration for RGBD salient object detection," in *The IEEE Conference on Computer Vision and Pattern Recognition*, 2019, pp. 3927–3936.
- [22] H. Chen and Y. Li, "Progressively complementarity-aware fusion network for RGB-D salient object detection," in *The IEEE Conference on Computer Vision and Pattern Recognition*, 2018, pp. 3051–3060.
- [23] H. Chen, Y. Li, and D. Su, "Multi-modal fusion network with multi-scale multi-path and cross-modal interactions for RGB-D salient object detection," *IEEE Transactions on Cybernetics*, vol. 86, pp. 376–385, 2019.
- [24] G. Li, Z. Liu, L. Ye, Y. Wang, and H. Ling, "Cross-Modal Weighting Network for RGB-D Salient Object Detection," in *European Conference on Computer Vision*, 2020.
- [25] Z. Liu, S. Shi, Q. Duan, W. Zhang, and P. Zhao, "Salient object detection for RGB-D image by single stream recurrent convolutional neural network," *Neurocomputing*, vol. 363, pp. 46–57, 2019.

[26] C. Zhu, X. Cai, K. Huang, T. H. Li, and G. Li, "Pdnet: Prior-model guided depth-enhanced network for salient object detection," in *IEEE International Conference on Multimedia and Expo*, 2019, pp. 199–204.

[27] Z. Wu, L. Su, and Q. Huang, "Cascaded partial decoder for fast and accurate salient object detection," in *The IEEE Conference on Computer Vision and Pattern Recognition*, 2019, pp. 3907–3916.

[28] J. Guo, T. Ren, and J. Bei, "Salient object detection for RGB-D image via saliency evolution," in *IEEE International Conference on Multimedia and Expo*, 2016, pp. 1–6.

[29] D. Feng, N. Barnes, S. You, and C. McCarthy, "Local background enclosure for RGB-D salient object detection," in *The IEEE Conference on Computer Vision and Pattern Recognition*, 2016, pp. 2343–2350.

[30] N. Wang and X. Gong, "Adaptive fusion for RGB-D salient object detection," *IEEE Access*, vol. 7, pp. 55 277–55 284, 2019.

[31] R. Cong, J. Lei, H. Fu, Q. Huang, X. Cao, and N. Ling, "HSCS: Hierarchical sparsity based co-saliency detection for RGBD images," *IEEE Transactions on Multimedia*, vol. 21, no. 7, pp. 1660–1671, 2019.

[32] H. Peng, B. Li, W. Xiong, W. Hu, and R. Ji, "RGBD salient object detection: a benchmark and algorithms," in *The European Conference on Computer Vision*, 2014, pp. 92–109.

[33] X. Fan, Z. Liu, and G. Sun, "Salient region detection for stereoscopic images," in *International Conference on Digital Signal Processing*, 2014, pp. 454–458.

[34] Y. Fang, J. Wang, M. Narwaria, P. Le Callet, and W. Lin, "Saliency detection for stereoscopic images," *IEEE Transactions on Image Processing*, vol. 23, no. 6, pp. 2625–2636, 2014.

[35] Y. Cheng, H. Fu, X. Wei, J. Xiao, and X. Cao, "Depth enhanced saliency detection method," in *International Conference on Internet Multimedia Computing and Service*, 2014, pp. 23–27.

[36] C. Zhu, G. Li, W. Wang, and R. Wang, "An innovative salient object detection using center-dark channel prior," in *The IEEE International Conference on Computer Vision Workshops*, 2017, pp. 1509–1515.

[37] D.-P. Fan, Z. Lin, Z. Zhang, M. Zhu, and M.-M. Cheng, "Rethinking RGB-D Salient Object Detection: Models, Data Sets, and Large-Scale Benchmarks," *IEEE Transactions on Neural Networks and Learning Systems*, 2020.

[38] T. Liu, Z. Yuan, J. Sun, J. Wang, N. Zheng, X. Tang, and H.-Y. Shum, "Learning to detect a salient object," *IEEE Transactions on Pattern Analysis and Machine Intelligence*, vol. 33, no. 2, pp. 353–367, 2010.

[39] R. Achanta, S. Hemami, F. Estrada, and S. Sussstrunk, "Frequency-tuned salient region detection," in *IEEE Conference on Computer Vision and Pattern Recognition*. IEEE, 2009, pp. 1597–1604.

[40] D.-P. Fan, M.-M. Cheng, J.-J. Liu, S.-H. Gao, Q. Hou, and A. Borji, "Salient objects in clutter: Bringing salient object detection to the foreground," in *The European Conference on Computer Vision*, 2018, pp. 186–202.

[41] G. Li and Y. Yu, "Deep contrast learning for salient object detection," in *IEEE Conference on Computer Vision and Pattern Recognition*, 2016, pp. 478–487.

[42] P. Zhang, D. Wang, H. Lu, H. Wang, and B. Yin, "Learning uncertain convolutional features for accurate saliency detection," in *The IEEE International Conference on Computer Vision*, 2017, pp. 212–221.

[43] X. Zhao, Y. Pang, L. Zhang, H. Lu, and L. Zhang, "Suppress and balance: A simple gated network for salient object detection," in *European Conference on Computer Vision*, 2020.

[44] L. Itti, C. Koch, and E. Niebur, "A model of saliency-based visual attention for rapid scene analysis," *IEEE Transactions on Pattern Analysis and Machine Intelligence*, vol. 20, no. 11, pp. 1254–1259, 1998.

[45] G. Li and Y. Yu, "Visual saliency based on multiscale deep features," in *The IEEE Conference on Computer Vision and Pattern Recognition*, 2015, pp. 5455–5463.

[46] M.-M. Cheng, J. Warrell, W.-Y. Lin, S. Zheng, V. Vineet, and N. Crook, "Efficient salient region detection with soft image abstraction," in *The IEEE International Conference on Computer vision*, 2013, pp. 1529–1536.

[47] S. Chen, X. Tan, B. Wang, H. Lu, X. Hu, and Y. Fu, "Reverse attention-based residual network for salient object detection," *IEEE Transactions on Image Processing*, vol. 29, pp. 3763–3776, 2020.

[48] X. Zhang, T. Wang, J. Qi, H. Lu, and G. Wang, "Progressive attention guided recurrent network for salient object detection," in *The IEEE Conference on Computer Vision and Pattern Recognition*, 2018, pp. 714–722.

[49] J. Su, J. Li, Y. Zhang, C. Xia, and Y. Tian, "Selectivity or invariance: Boundary-aware salient object detection," in *The IEEE International Conference on Computer Vision*, 2019, pp. 3799–3808.

[50] L. Zhang, J. Wu, T. Wang, A. Borji, G. Wei, and H. Lu, "A multistage refinement network for salient object detection," *IEEE Transactions on Image Processing*, vol. 29, pp. 3534–3545, 2020.

[51] H. Li, G. Chen, G. Li, and Y. Yu, "Motion guided attention for video salient object detection," in *The IEEE International Conference on Computer Vision*, 2019, pp. 7274–7283.

[52] P. Zhang, D. Wang, H. Lu, H. Wang, and X. Ruan, "Amulet: Aggregating multi-level convolutional features for salient object detection," in *The IEEE International Conference on Computer Vision*, 2017, pp. 202–211.

[53] B. Wang, Q. Chen, M. Zhou, Z. Zhang, X. Jin, and K. Gai, "Progressive feature polishing network for salient object detection," in *The AAAI Conference on Artificial Intelligence*, 2020, pp. 12 128–12 135.

[54] J. Wei, S. Wang, and Q. Huang, "F3net: Fusion, feedback and focus for salient object detection," in *The AAAI Conference on Artificial Intelligence*, 2020.

[55] Y. Pan, T. Yao, H. Li, and T. Mei, "Video captioning with transferred semantic attributes," in *The IEEE Conference on Computer Vision and Pattern Recognition*, 2017, pp. 984–992.

[56] Z. Zhang, S. Fidler, and R. Urtasun, "Instance-level segmentation for autonomous driving with deep densely connected mrfs," in *The IEEE Conference on Computer Vision and Pattern Recognition*, 2016, pp. 669–677.

[57] N. Xu, B. L. Price, S. Cohen, J. Yang, and T. S. Huang, "Deep interactive object selection," in *The IEEE Conference on Computer Vision and Pattern Recognition*, 2016, pp. 373–381.

[58] S. Xie and Z. Tu, "Holistically-nested edge detection," *International Journal of Computer Vision*, vol. 125, no. 1-3, pp. 3–18, 2017.

[59] Y. Zhuge, G. Yang, P. Zhang, and H. Lu, "Boundary-guided feature aggregation network for salient object detection," *IEEE Signal Processing Letters*, vol. 25, no. 12, pp. 1800–1804, 2018.

[60] J.-X. Zhao, J.-J. Liu, D.-P. Fan, Y. Cao, J. Yang, and M.-M. Cheng, "EGNet: Edge guidance network for salient object detection," in *The IEEE International Conference on Computer Vision*, 2019, pp. 8779–8788.

[61] Z. Wu, L. Su, and Q. Huang, "Stacked cross refinement network for edge-aware salient object detection," in *The IEEE International Conference on Computer Vision*, 2019, pp. 7264–7273.

[62] K. Desingh, K. Krishna, D. Rajanand, and C. Jawahar, "Depth really matters: Improving visual salient region detection with depth," in *British Machine Vision Conference*, 2013, pp. 1–11.

[63] A. Ciptadi, T. Hermans, and J. M. Rehg, "An in depth view of saliency," in *British Machine Vision Conference*, 2013, pp. 1–11.

[64] L. Qu, S. He, J. Zhang, J. Tian, Y. Tang, and Q. Yang, "RGBD salient object detection via deep fusion," *IEEE Transactions on Image Processing*, vol. 26, no. 5, pp. 2274–2285, 2017.

[65] R. Cong, J. Lei, H. Fu, J. Hou, Q. Huang, and S. Kwong, "Going from RGB to RGBD saliency: A depth-guided transformation model," *IEEE Transactions on Cybernetics*, pp. 1–13, 2019.

[66] R. Shigematsu, D. Feng, S. You, and N. Barnes, "Learning RGB-D salient object detection using background enclosure, depth contrast, and top-down features," in *The IEEE International Conference on Computer Vision Workshops*, 2017, pp. 2749–2757.

[67] R. Ju, L. Ge, W. Geng, T. Ren, and G. Wu, "Depth saliency based on anisotropic center-surround difference," in *IEEE International Conference on Image Processing*, 2014, pp. 1115–1119.

[68] K. He, X. Zhang, S. Ren, and J. Sun, "Deep residual learning for image recognition," in *The IEEE Conference on Computer Vision and Pattern Recognition*, 2016, pp. 770–778.

[69] J. Han, H. Chen, N. Liu, C. Yan, and X. Li, "CNNs-Based RGB-D saliency detection via cross-view transfer and multiview fusion," *IEEE Transactions on Cybernetics*, vol. 48, no. 11, pp. 3171–3183, 2018.

[70] J. Zhang, D.-P. Fan, Y. Dai, S. Anwar, F. Sadat Saleh, T. Zhang, and N. Barnes, "UC-Net: Uncertainty Inspired RGB-D Saliency Detection via Conditional Variational Autoencoders," in *The IEEE Conference on Computer Vision and Pattern Recognition*, 2020, pp. 8582–8591.

[71] Y. Wang, Y. Li, J. H. Elder, H. Lu, and R. Wu, "Synergistic saliency and depth prediction for RGB-D saliency detection," *arXiv preprint arXiv:2007.01711*, 2020.

[72] K. F. Fu, D.-P. Fan, G.-P. Ji, and Q. Zhao, "JL-DCF: Joint Learning and Densely-Cooperative Fusion Framework for RGB-D Salient Object Detection," in *The IEEE Conference on Computer Vision and Pattern Recognition*, 2020, pp. 3052–3062.

[73] A. Luo, X. Li, F. Yang, Z. Jiao, H. Cheng, and S. Lyu, "Cascade Graph Neural Networks for RGB-D Salient Object Detection," in *European Conference on Computer Vision*, 2020.

[74] X. Zhao, L. Zhang, Y. Pang, H. Lu, and L. Zhang, "A Single Stream Network for Robust and Real-time RGB-D Salient Object Detection," in *European Conference on Computer Vision*, 2020.

[75] C. Li, R. Cong, Y. Piao, Q. Xu, and C. C. Loy, "RGB-D Salient Object Detection with Cross-Modality Modulation and Selection," in *European Conference on Computer Vision*, 2020.

[76] T. Zhou, D.-P. Fan, M.-M. Cheng, J. Shen, and L. Shao, "RGB-D Salient Object Detection: A Survey," *arXiv preprint arXiv:2008.00230*, 2020.

[77] S. Liu, D. Huang, and Y. Wang, "Receptive field block net for accurate and fast object detection," in *The European Conference on Computer Vision*, 2018, pp. 404–419.

[78] X. Hu, K. Yang, L. Fei, and K. Wang, "ACNet: Attention Based Network to Exploit Complementary Features for RGBD Semantic Segmentation," in *IEEE International Conference on Image Processing*, 2019, pp. 1440–1444.

[79] Q. Chen and V. Koltun, "Photographic image synthesis with cascaded refinement networks," in *The IEEE Conference on Computer Vision and Pattern Recognition*, 2017, pp. 1511–1520.

[80] T. Wang, A. Borji, L. Zhang, P. Zhang, and H. Lu, "A stagewise refinement model for detecting salient objects in images," in *The IEEE International Conference on Computer Vision*, 2017, pp. 4039–4048.

[81] Z. Deng, X. Hu, L. Zhu, X. Xu, J. Qin, G. Han, and P.-A. Heng, "R3Net: Recurrent residual refinement network for saliency detection," in *International Joint Conference on Artificial Intelligence*, 2018, pp. 684–690.

[82] S. Woo, J. Park, J.-Y. Lee, and I. So Kweon, "CBAM: Convolutional block attention module," in *The European Conference on Computer Vision*, 2018, pp. 3–19.

[83] M. Oquab, L. Bottou, I. Laptev, and J. Sivic, "Is object localization for free? - weakly-supervised learning with convolutional neural networks," in *The IEEE Conference on Computer Vision and Pattern Recognition*, 2015, pp. 685–694.

[84] Y. Niu, Y. Geng, X. Li, and F. Liu, "Leveraging stereopsis for saliency analysis," in *The IEEE Conference on Computer Vision and Pattern Recognition*, 2012, pp. 454–461.

[85] N. Li, J. Ye, Y. Ji, H. Ling, and J. Yu, "Saliency detection on light field," in *The IEEE Conference on Computer Vision and Pattern Recognition*, 2014, pp. 2806–2813.

[86] C. Zhu and G. Li, "A three-pathway psychobiological framework of salient object detection using stereoscopic technology," in *The IEEE International Conference on Computer Vision Workshops*, 2017, pp. 3008–3014.

[87] B. Steiner, Z. DeVito, S. Chintala, S. Gross, A. Paszke, F. Massa, A. Lerer, G. Chanan, Z. Lin, E. Yang *et al.*, "PyTorch: An imperative style, high-performance deep learning library," in *Advances in Neural Information Processing Systems*, 2019, pp. 8024–8035.

[88] A. Krizhevsky, I. Sutskever, and G. E. Hinton, "Imagenet classification with deep convolutional neural networks," in *Advances in Neural Information Processing Systems*, 2012, pp. 1106–1114.

[89] D. P. Kingma and J. Ba, "Adam: A method for stochastic optimization," in *International Conference on Learning Representations*, 2015.

[90] Y. Piao, Z. Rong, M. Zhang, W. Ren, and H. Lu, "A2dele: Adaptive and Attentive Depth Distiller for Efficient RGB-D Salient Object Detection," in *IEEE Conference on Computer Vision and Pattern Recognition*, 2020, pp. 9060–9069.

[91] M. Zhang, W. Ren, Y. Piao, Z. Rong, and H. Lu, "Select, Supplement and Focus for RGB-D Saliency Detection," in *IEEE Conference on Computer Vision and Pattern Recognition*, 2020, pp. 3472–3481.

[92] D.-P. Fan, M.-M. Cheng, Y. Liu, T. Li, and A. Borji, "Structure-measure: A new way to evaluate foreground maps," in *The IEEE International Conference on Computer Vision*, 2017, pp. 4548–4557.

[93] D.-P. Fan, C. Gong, Y. Cao, B. Ren, M.-M. Cheng, and A. Borji, "Enhanced-alignment measure for binary foreground map evaluation," in *International Joint Conference on Artificial Intelligence*, 2018, pp. 698–704.

[94] R. Achanta, S. Hemami, F. Estrada, and S. Sussstrunk, "Frequency-tuned salient region detection," in *The IEEE Conference on Computer Vision and Pattern Recognition*, 2009, pp. 1597–1604.

[95] C. Zhu, G. Li, X. Guo, W. Wang, and R. Wang, "A multilayer backpropagation saliency detection algorithm based on depth mining," in *International Conference on Computer Analysis of Images and Patterns*, 2017, pp. 14–23.

[96] R. Cong, J. Lei, C. Zhang, Q. Huang, X. Cao, and C. Hou, "Saliency detection for stereoscopic images based on depth confidence analysis and multiple cues fusion," *IEEE Signal Processing Letters*, vol. 23, no. 6, pp. 819–823, 2016.

[97] F. Liang, L. Duan, W. Ma, Y. Qiao, Z. Cai, and L. Qing, "Stereoscopic saliency model using contrast and depth-guided-background prior," *Neurocomputing*, vol. 275, pp. 2227–2238, 2018.

[98] J. Ren, X. Gong, L. Yu, W. Zhou, and M. Ying Yang, "Exploiting global priors for RGB-D saliency detection," in *The IEEE Conference on Computer Vision and Pattern Recognition Workshops*, 2015, pp. 25–32.

[99] H. Song, Z. Liu, H. Du, G. Sun, O. Le Meur, and T. Ren, "Depth-aware salient object detection and segmentation via multiscale discriminative saliency fusion and bootstrap learning," *IEEE Transactions on Image Processing*, vol. 26, no. 9, pp. 4204–4216, 2017.

[100] K. Simonyan and A. Zisserman, "Very deep convolutional networks for large-scale image recognition," *arXiv preprint arXiv:1409.1556*, 2014.

[101] N. Liu, J. Han, and M.-H. Yang, "PiCANet: Learning Pixel-Wise Contextual Attention for Saliency Detection," in *The IEEE Conference on Computer Vision and Pattern Recognition*, 2018, pp. 3089–3098.

[102] J. Yang and M.-H. Yang, "Top-down visual saliency via joint crf and dictionary learning," *IEEE Transactions on Pattern Analysis and Machine Intelligence*, vol. 39, no. 3, pp. 576–588, 2016.

[103] W. Wang, S. Zhao, J. Shen, S. C. Hoi, and A. Borji, "Salient object detection with pyramid attention and salient edges," in *The IEEE Conference on Computer Vision and Pattern Recognition*, 2019, pp. 1448–1457.

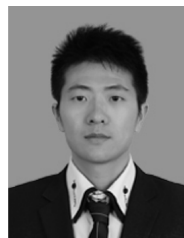
[104] Y. Zeng, Y. Zhuge, H. Lu, and L. Zhang, "Joint learning of saliency detection and weakly supervised semantic segmentation," in *The IEEE International Conference on Computer Vision*, 2019, pp. 7223–7233.

[105] N. Otsu, "A threshold selection method from gray-level histograms," *IEEE Transactions on Systems, Man, and Cybernetics*, vol. 9, no. 1, pp. 62–66, 1979.

[106] P. Krähenbühl and V. Koltun, "Efficient inference in fully connected crfs with gaussian edge potentials," in *Advances in Neural Information Processing Systems*, 2011, pp. 109–117.



Yingjie Zhai is currently a PhD student with the Computer Vision Lab at College of Computer Science, Nankai University, Tianjin, China. His current research interests include deep learning and computer vision, especially salient object detection and image restoration. He is a Student Member of IEEE.



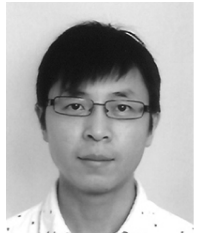
Deng-Ping Fan received his PhD degree from the Nankai University and then he joined Inception Institute of Artificial Intelligence (IIAI) in 2019. He has published about 20 top journal and conference papers such as CVPR, ICCV, etc. His research interests include computer vision, deep learning, and saliency detection, especially on co-salient object detection, RGB salient object detection, RGB-D salient object detection, and video salient object detection.



Jufeng Yang received his PhD degree from Nankai University, Tianjin, China, in 2009. He is currently a full professor in the Department of Computer Science and Technology, Nankai University and was a visiting scholar with the Vision and Learning Lab, University of California, Merced, USA, from 2015 to 2016. His research falls in the field of computer vision, machine learning and multimedia. His recent interests include affective computing, image retrieval, fine-grained classification and medical imaging. He served as an organizing committee chair of CCCV 2017 and CVM 2017. He was a committee member of CVPR, ICCV, ECCV and a reviewer of various international journals.



Ali Borji received the PhD degree in cognitive neurosciences from the Institute for Studies in Fundamental Sciences (IPM), Tehran, IRAN in 2009. He had a postdoc at the University of Southern California from 2010 to 2014. He is currently with HCL America, NYC. His research interests include visual attention, visual search, object and scene recognition, machine learning, neurosciences, and biologically plausible vision models.



Ling Shao is the CEO and Chief Scientist of the Inception Institute of Artificial Intelligence (IIAI), Abu Dhabi, United Arab Emirates. His research interests include computer vision, machine learning and medical imaging. He is an associate editor of *IEEE TRANSACTIONS ON IMAGE PROCESSING*, *IEEE TRANSACTIONS ON NEURAL NETWORKS AND LEARNING SYSTEMS*, and several other journals. He is a fellow of the International Association of Pattern Recognition, the Institution of Engineering and Technology and the British Computer Society.



Junwei Han is currently a Full Professor with Northwestern Polytechnical University, Xian, China. His research interests include computer vision, multimedia processing, and brain imaging analysis. He is an Associate Editor of *IEEE Trans. on Human-Machine Systems*, *Neurocomputing*, and *Multidimensional Systems and Signal Processing*.



Liang Wang received both the BEng and MEng degrees from Anhui University in 1997 and 2000, respectively, and the PhD degree from the Institute of Automation, Chinese Academy of Sciences (CASIA) in 2004. From 2004 to 2010, he was a research assistant at Imperial College London, United Kingdom, and Monash University, Australia, a research fellow at the University of Melbourne, Australia, and a lecturer at the University of Bath, United Kingdom, respectively. Currently, he is a full professor of the Hundred Talents Program at the National Lab of Pattern Recognition, CASIA. His major research interests include machine learning, pattern recognition, and computer vision. He serves as an Associate Editor of *IEEE TPAMI* and *IEEE TIP*. He is a Fellow of the IEEE and IAPR.